J. Fluid Mech. (2017), *vol.* 829, *pp.* 751–779. © Cambridge University Press 2017
doi:10.1017/jfm.2017.579

Influence of large-scale motions on the frictional drag in a turbulent boundary layer

Jinyul Hwang[1] **and Hyung Jin Sung**[1,†]

[1]Department of Mechanical Engineering, KAIST, 291 Daehak-ro, Yuseong-gu, Daejeon 34141, Korea

(Received 30 August 2016; revised 31 July 2017; accepted 13 August 2017;
first published online 26 September 2017)

Direct numerical simulation data of a turbulent boundary layer ($Re_\tau = 1000$) were used to investigate the large-scale influences on the vortical structures that contribute to the local skin friction. The amplitudes of the streamwise and wall-normal swirling strengths (λ_x and λ_y) were conditionally sampled by measuring the large-scale streamwise velocity fluctuations (u_l). In the near-wall region, the amplitudes of λ_x and λ_y decreased under negative u_l rather than under positive u_l. This behaviour arose from the spanwise motions within the footprints of the large-scale low-speed ($u_l < 0$) and high-speed structures ($u_l > 0$). The intense spanwise motions under the footprint of positive u_l noticeably strengthened the small-scale spanwise velocity fluctuations (w_s) below the centre of the near-wall vortical structures as compared to w_s within the footprint of negative u_l. The streamwise and wall-normal components were attenuated or amplified around the modulated vortical motions, which in turn led to the dependence of the swirling strength on the u_l event. We quantified the contribution of the modulated vortical motions $\langle -w\omega_y \rangle$, which were related to a change-of-scale effect due to the vortex-stretching force, to the local skin friction. In the near-wall region, intense values of $\langle -w\omega_y \rangle$ were observed for positive u_l. By contrast, these values were low for negative u_l, in connection with the amplification of w_s and λ_y by the strong spanwise motions of the positive u_l. The resultant skin friction induced by the amplified vortical motions within $u_l^+ > 2$ was responsible for 15 % of the total skin friction generated by the change-of-scale effect. Finally, we applied this analysis to a drag-reduced flow and found that the amplified vortical motions within the footprint of positive u_l were markedly diminished, which ultimately contributed to the total drag reduction.

Key words: turbulence simulation, turbulent boundary layers, turbulent flows

1. Introduction

In turbulent boundary layers (TBLs), the outer large-scale structures play a significant role in producing the turbulent kinetic energy and in momentum transfer. These organized motions scale with the outer length scale δ, where δ is the channel half-height, the pipe radius or the 99 % boundary layer thickness. Experimental and numerical studies confirmed the presence of large-scale structures in wall-bounded flows. These structures contribute substantially to the turbulent kinetic energy and

† Email address for correspondence: hjsung@kaist.ac.kr

the Reynolds shear stress in internal flows (Liu, Adrian & Hanratty 2001; Guala, Hommema & Adrian 2006; Balakumar & Adrian 2007; Wu, Baltzer & Adrian 2012; Lee & Sung 2013; Ahn *et al.* 2015) and in TBLs (Ganapathisubramani, Longmire & Marusic 2003; Balakumar & Adrian 2007; Hutchins & Marusic 2007*a*; Lee & Sung 2011). In addition, the footprint of the large-scale structures extends to the near-wall region and thus induces the large scales nearer to the wall (Hutchins & Marusic 2007*a*). The presence of the large scales in the near-wall region causes a scaling failure in the inner-normalized streamwise turbulence intensity (del Álamo & Jiménez 2003; Hoyas & Jiménez 2006; Hutchins & Marusic 2007*a*), highlighting that the outer large-scale structures and the near-wall region are interlinked.

1.1. *Near-wall influence of large-scale structures*

A noteworthy feature of the large-scale structures is their influence on the small scales, which is not merely a superposition in the near-wall region. By separating the fluctuating signals into high- and low-frequency components, previous studies (Brown & Thomas 1977; Bandyopadhyay & Hussain 1984) reported coupling between the large-scale and small-scale fluctuations. Recently, Hutchins & Marusic (2007*b*) showed that the large-scale streamwise velocity fluctuations modulate the amplitude of the small scales in the near-wall region. Using the Hilbert transform, Mathis, Hutchins & Marusic (2009) quantified the amplitude modulation (AM) effects of the large scales. They defined the AM coefficient as indicative of the correlation between the large-scale streamwise velocity fluctuations and the envelope of small-scale streamwise velocity fluctuations. The AM coefficient is positive in the near-wall region and becomes negative above the wall-normal position at which the outer peak is observed in the premultiplied streamwise energy spectra. Other methods were employed in several studies (Chung & McKeon 2010; Schlatter & Örlü 2010*b*; Guala, Metzger & McKeon 2011; Hutchins *et al.* 2011), which found the AM effects on small scales due to the large-scale structures in a manner analogous to that observed in Mathis *et al.* (2009). Talluru *et al.* (2014) extended this view to quantify the AM of the small-scale wall-normal and spanwise velocity fluctuations and revealed a trend similar to that observed among the streamwise components. Bernardini & Pirozzoli (2011) computed the two-point AM correlation along the wall-normal direction and observed the presence of an off-diagonal positive peak related to the influence of the outer large-scale structures on the near-wall small scales.

Although the aforementioned works characterize the AM effects induced by the large-scale structures, these methods do not differentiate the influences of large-scale low- or high-speed events. The large-scale structures in the outer region assume the form of long low-speed regions flanked by high-speed regions (Hutchins & Marusic 2007*a*; Monty *et al.* 2007), whereas the low-speed regions are longer along their streamwise extents as compared to the high-speed regions (Dennis & Nickels 2011; Lee & Sung 2013; Hwang *et al.* 2016*b*). Furthermore, the footprint of the high-speed structures is wider than that of the low-speed structures due to the presence of opposing spanwise motions induced by the associated large-scale circulations, which are either congregative or dispersive (Hwang *et al.* 2016*b*). Toh & Itano (2005) addressed that near-wall structures congregate and separate under the large-scale low- and high-speed structures in the outer region. The large-scale roll motions of the low-speed structures induce the migration of the near-wall structures under the outer ejections, whereas those of the high-speed structures generate a separation region under the outer sweeps. The difference among the large-scale low- and high-speed

events is associated with the asymmetric contributions to the Reynolds stresses in the near-wall region (Agostini & Leschziner 2014; Hwang *et al.* 2016*b*) and with the attenuation or amplification of the small scales depending on the sign of the large-scale fluctuations observed in the instantaneous fluctuating signals (Hutchins & Marusic 2007*b*). To account for these observations, therefore, it is necessary to examine the AM effect in terms of the sign of the large scales.

1.2. *Influence of large-scale structures on the vortical motions*

For the streamwise velocity components, Ganapathisubramani *et al.* (2012) examined the effect of AM on the sign of the large scales in the TBL. They computed the variance of the small-scale streamwise velocity fluctuations conditioned on the strength of the large-scale fluctuations along the wall-normal direction. In the near-wall region, the variance of the small scales conditioned on the negative large scales is lower than that conditioned on the positive large scales, whereas the former exceeds the latter as the wall-normal position increased. Hutchins & Marusic (2007*b*) observed the amplification and attenuation of all the velocity fluctuations and Reynolds shear stress in the instantaneous fluctuating signals during the large-scale high-speed and low-speed regions. The influence of the large scales on the dissipative scales was reported by Guala *et al.* (2011). In addition, Ganapathisubramani *et al.* (2012) characterized the frequency modulation effect by the large scales below $y^+ = 100$ by counting the number of occurrences of local maxima and minima in the small-scale fluctuating signals. Since the vortical structures are responsible for small-scale activities in the near-wall region, these aforementioned studies suggested that the amplitudes of the vortical motions could be influenced by the strength of the large scales.

Hutchins & Marusic (2007*b*) showed the variation of the swirling strength around the outer low-speed event ($y^+ = 150$) that the magnitude of the swirling strength is reduced under the lower part of the large-scale low-speed structures, while this trend reverses above the reference wall-normal position. However, the event was chosen as the negative streamwise velocity fluctuations, and not decomposed into the small and large scales. As mentioned earlier, the footprints of the large-scale structures and their induced spanwise motions are asymmetric between the low- and high-speed events (Hwang *et al.* 2016*b*) and the AM effect of the large scales on the small scales depends on the sign of the large scales (Ganapathisubramani *et al.* 2012). These results indicate that the large-scale high-speed structures are not just the reversed features of the large-scale low-speed ones. There is a great interest in exploring the AM of the swirling strength by focusing on the large-scale low- and high-speed events.

Furthermore, although the AM of the vortical motions can be expected from the AM of the small-scale velocity fluctuations, the relationship between the modulated velocity fluctuations and the vortical motions has not yet been elucidated. In order to address this issue, we examine the conditionally averaged vortical structures under the influence of the large-scale structures and the associated fluctuating velocity fields. Toward this end, high-resolution direct numerical simulation (DNS) data collected over a large domain are required. Jeong *et al.* (1997) applied a similar approach to the streamwise vortical structures in a buffer region ($y^+ < 60$). By conditionally averaging the λ_2, proposed by Jeong & Hussain (1995), they revealed the spatial configurations of the structures and the associated intercomponent energy transfer. Although the conditionally averaged structures do not provide sufficient information to explain

their dynamics, the educed structures represent the statistically significant structural properties and capture the instantaneous kinematic features in the near-wall region (Robinson 1991). Analysing the conditionally averaged velocity fields associated with the near-wall vortical structures in this manner allows us to determine the relationship between the modulated velocity fields and the vortical structures.

1.3. *Contribution of vortical motions to skin friction*

The AM behaviour of the vortical motions is expected to influence the dependence of the local skin friction on the presence of large scales, because the vortical structures play a significant role in the frictional drag (Robinson 1991) and in the near-wall sustaining cycle (Hamilton, Kim & Waleffe 1995; Jiménez & Pinelli 1999). The outer large-scale motions effect on the wall shear stress (Abe, Kawamura & Choi 2004; Schlatter *et al.* 2009). In addition, the contributions of the large scales to the fluctuating wall-shear stress increase with the presence of the outer peak (Örlü & Schlatter 2011). Using the conditional averaging analysis, Hutchins *et al.* (2011) observed that a large-scale low skin-friction event at the wall is associated with the footprint of the large-scale low-speed structures. Ganapathisubramani *et al.* (2012) interpreted these observations that the large-scale structures have their footprints in the wall-shear stress, which varies the local Re_τ in the near-wall region. This interpretation is consistent with the theoretical description of large-scale effects addressed by Chernyshenko, Marusic & Mathis (2012) in which the total skin friction and velocity are scaled in the large-scale fluctuating components, representing the superposition and modulation effects of large scales. An important advantage of the AM behaviour is its utility for predicting near-wall turbulence and for controlling flow. The prediction of the near-wall turbulence using a mathematical model, which includes the AM effect and superposition of large scales, was suggested in Marusic, Mathis & Hutchins (2010). In addition, Mathis *et al.* (2013) extended this approach to develop a predictive model for the streamwise wall-shear-stress fluctuations, contributing to the skin-friction coefficient (C_f). However, flow control using the AM phenomenon has not yet been reported. Flow control using the AM phenomenon of the large-scale structures relies on two developments: (i) elucidation of the mechanism by which large-scale low- or high-speed structures attenuate or amplify the small scales (see also § 5); and (ii) quantification of the AM effects on the skin-friction coefficient. A quantitative analysis of the AM effects on the skin friction, in particular, could enable the evaluation of new control strategies based on the AM behaviours of large-scale motions.

The contribution of the modulated vortical motions to C_f could be quantified by using a new decomposition method for C_f, as suggested by Yoon *et al.* (2016*a*). This method provides a direct measure of the contributions of the velocity–vorticity correlations (i.e. the cross-correlation between the wall-normal velocity and the spanwise vorticity fluctuations $\langle v\omega_z\rangle$, and between the spanwise velocity and the wall-normal vorticity fluctuations $\langle -w\omega_y\rangle$). The first term $\langle v\omega_z\rangle$ represents a body force arising from the transport of ω_z by v (advective vorticity transport). The second term $\langle -w\omega_y\rangle$ is interpreted as a vortex-stretching force associated with the change-of-scale effect (Tennekes & Lumley 1972). In addition, $\langle -w\omega_y\rangle$ is closely related to the AM of the small scales by the large-scale motions, because the spectral contribution of large-scale wavelengths to $\langle -w\omega_y\rangle$ increases with Re_τ in connection with the outward movement of the onset of the log region (Chin *et al.* 2014). The contribution of the modulated vortical motions to the skin friction could

Re_θ	$(L_x/\delta_0, L_y/\delta_0, L_z/\delta_0)$	(N_x, N_y, N_z)	Δx^+	Δy^+_{min}	Δy^+_{max}	Δz^+	Δt^+
109–3240	(2300, 100, 100)	(13 313, 541, 769)	5.49	0.159	9.56	4.13	0.0504

TABLE 1. Parameters used in the simulations. L_i and N_i indicate the domain size and the number of grid points, respectively. The grid sizes were Δx^+ and Δz^+. The minimum and maximum grid sizes in the wall-normal direction were Δy^+_{min} and Δy^+_{max}, respectively, and Δt^+ is the time step. The inner-normalized resolutions were taken at $Re_\tau = 1000$.

be quantified by computing the contribution of $\langle -w\omega_y \rangle$ to C_f, which enables a quantitative discussion of the skin friction due to the AM of vortical structures.

The objective of the present study is to investigate the influence of large-scale low- and high-speed structures on the vortical motions associated with the local skin friction. Our approach relies on an analysis of DNS data obtained from a TBL at $Re_\tau = 1000$. The conditional sampling technique used to identify large-scale low- and high-speed events is provided in § 3. In § 4, the amplitudes of the streamwise and wall-normal vortical structures are computed based on the strengths of the large-scale fluctuations. In § 5, the vortical structures and the associated velocity fields are conditionally averaged in terms of the strength of the large scales. The amplification or attenuation of the vortical motions is intrinsically linked to the AM of the velocity fluctuations, which arise from the near-wall spanwise motions induced by large-scale structures. In § 6, we quantify the contribution of the modulated vortical motions to the local skin friction, which provides a rational basis for controlling turbulence using the AM behaviour of large-scale structures. Finally, a summary is provided in § 7.

2. Computational details

The Navier–Stokes equations for incompressible flow were solved using the fractional step method by Kim, Baek & Sung (2002). In the present work, x, y and z denote the streamwise, wall-normal and spanwise directions, respectively, and the associated velocity components are $\tilde{u}$, $\tilde{v}$ and $\tilde{w}$. Capital letters or an angle bracket $\langle\cdot\rangle$ are used to indicate the mean quantities and lower-case letters represent the fluctuating components (e.g. $u = \tilde{u} - U$). The superscript $+$ denotes quantities normalized by the viscous scales, i.e. the friction velocity u_τ and the kinematic viscosity ν. We performed a DNS of a zero pressure gradient boundary layer over a flat plate. The parameters of the current simulation are summarized in table 1. The inlet Reynolds number was defined as $Re_{\delta_0} \equiv U_\infty \delta_0/\nu = 800$ based on the free-stream velocity U_∞ and the 99 % boundary layer thickness δ_0. The grid spacing was uniform along the streamwise and spanwise directions. A hyperbolic tangent function was used in the wall-normal direction. The no-slip boundary condition was applied at the wall, and the top boundary condition was $\tilde{u} = U_\infty$, $\partial\tilde{v}/\partial y = 0$ and $\tilde{w} = 0$. In the spanwise direction, periodic boundary conditions were imposed. The convective boundary condition was applied at the exit according to $\partial\tilde{u}/\partial t + c(\partial\tilde{u}/\partial x) = 0$, where c is the local bulk velocity. The inflow condition was set as a superposition of the Blasius velocity profile and the isotropic free-stream turbulence. The free-stream turbulence was generated by the Orr–Sommerfeld and Squire modes in the wall-normal direction and Fourier modes in time and in the spanwise direction (Jacobs & Durbin 2001). The turbulent intensity of the free-stream turbulence was 5 % and was imposed on the Blasius profile up to $y = 2\delta_0$ to induce the rapid decay of the free-stream turbulence in the downstream direction. The present simulation resolved the turbulent flow through

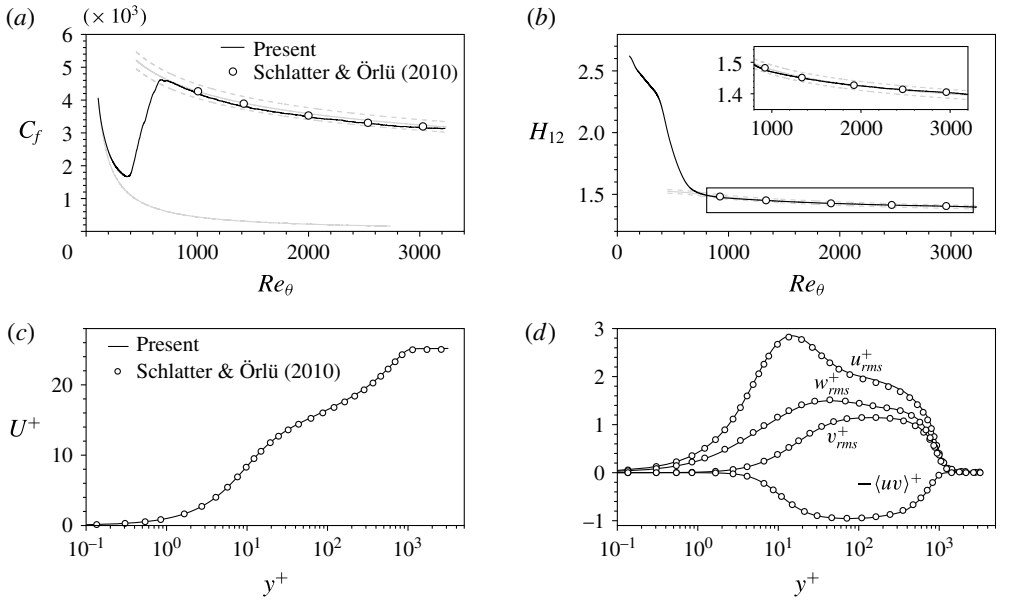

FIGURE 1. (*a*) Skin-friction coefficient C_f; laminar and turbulent C_f predictions for zero pressure gradient TBL (grey solid line). The dashed lines indicate a $\pm 5\,\%$ tolerance of turbulent C_f prediction. (*b*) Shape factor H_{12}. The grey solid line represents the integration of the composite profile by Chauhan *et al.* (2009) and the dashed lines indicate a $\pm 1\,\%$ tolerance. Turbulence statistics at $Re_\theta \approx 3030$: (*c*) mean streamwise velocity; (*d*) r.m.s. of the turbulence intensities and the Reynolds shear stress.

the bypass transition. Therefore, the velocity and pressure fields were obtained in a single long domain. The boundary layer was spatially developing with the Reynolds number based on the momentum thickness, $Re_\theta = 109$–3240. The simulation was run using 512 cores on the Tachyon II (SUN B6275) KISTI supercomputer. The total averaging time used to ascertain the convergence of statistics was 10 200 viscous time units at $Re_\tau = 1000$. To validate the present data, the integral quantities, such as the skin-friction coefficient (C_f) and the shape factor (H_{12}), are shown in figure 1(*a*,*b*). The profiles of C_f and H_{12} obtained from the present DNS are plotted with the 1/7-power law of C_f (Smits, Matheson & Joubert 1983) and with the correlation of H_{12} (Chauhan, Monkewitz & Nagib 2009). The profiles of the present data lay within the tolerance and were in excellent agreement with the profiles reported by Schlatter & Örlü (2010*a*). In addition, the inner-normalized profiles of the mean streamwise velocity and Reynolds stresses at $Re_\theta = 3030$ were in good agreement with those reported in previous study (figure 1*c*,*d*).

3. Conditional sampling

Figure 2 plots the premultiplied spanwise spectrum of u at $Re_\tau \approx 1000$ across the wall-normal direction. Here, λ_z indicates the spanwise wavelength. Two peaks were observed and their positions were marked by the cross symbols. An inner peak appeared at $(y^+, \lambda_z^+) = (13, 120)$, indicating the self-sustaining cycle of the near-wall region (Hamilton *et al.* 1995; Jiménez & Pinelli 1999). In addition, a secondary peak was located at $(y/\delta, \lambda_z/\delta) = (0.18, 0.75)$. This outer peak represented

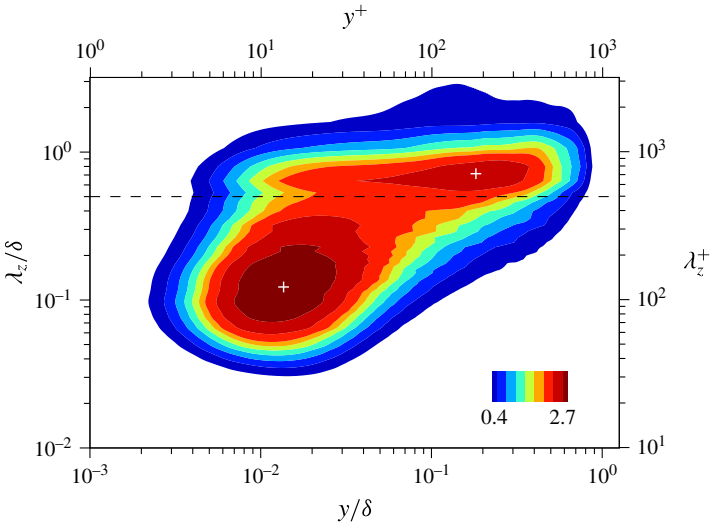

FIGURE 2. (Colour online) Premultiplied spanwise spectrum of the streamwise velocity fluctuations at $Re_\tau \approx 1000$. The dashed line indicates $\lambda_z/\delta = 0.5$. The cross symbols indicate the inner and outer sites at $(y^+ = 13,\ \lambda_z^+ = 120)$ and $(y/\delta = 0.18,\ \lambda_z/\delta = 0.75)$, respectively.

a spectral signature of the superstructures, similar to that observed in the premultiplied streamwise spectrum of u (Hutchins & Marusic 2007*a*). Although the Reynolds number of the present TBL was relatively low compared to the experiment, these two energy lobes could be demarcated based on the spanwise wavelength. The streamwise velocity fluctuations were separated into small (u_s) and large scales (u_l) in the spanwise direction with the cutoff wavelength of $\lambda_z/\delta = 0.5$ (Bernardini & Pirozzoli 2011; Ahn *et al.* 2013). The influence of the cutoff wavelength is examined in appendix A and was found to be insignificant.

As mentioned in the introduction, the AM of all the small-scale velocity fluctuations leads us to hypothesize that the vortical structures, which are the dominant coherent structures in the near-wall region, are affected by the outer large-scale motions. Hence, a conditional sampling analysis was applied to the vortical structures to examine the influence of the strength of u_l. The vortical structures were identified by the swirling strength (λ_{ci}), defined as the imaginary part of the eigenvalue of the velocity gradient tensor (Zhou *et al.* 1999). The streamwise and wall-normal swirling strength ($\lambda_{ci,x}$ and $\lambda_{ci,y}$) could be computed using the two-dimensional velocity gradient tensor (Adrian, Christensen & Liu 2000),

$$D_{ij}^{2D} = \begin{bmatrix} \dfrac{\partial u_i}{\partial x_i} & \dfrac{\partial u_i}{\partial x_j} \\ \dfrac{\partial u_j}{\partial x_i} & \dfrac{\partial u_j}{\partial x_j} \end{bmatrix}. \tag{3.1}$$

For example, $\lambda_{ci,x}$ ($i = 2$ and $j = 3$) and $\lambda_{ci,y}$ ($i = 1$ and $j = 3$). Furthermore, the sense of the rotation was demarcated by multiplying the swirling strength by the sign of the vorticity fluctuations (Tomkins & Adrian 2003),

$$\lambda_x = \lambda_{ci,x}\frac{\omega_x}{|\omega_x|}, \quad \lambda_y = \lambda_{ci,y}\frac{\omega_y}{|\omega_y|}. \tag{3.2a,b}$$

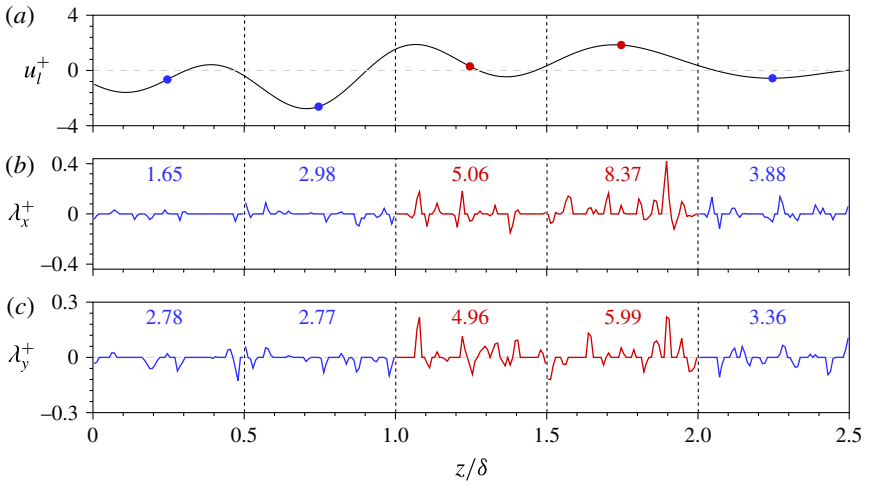

FIGURE 3. (Colour online) Near-wall fluctuating signals at $y^+ = 14.5$. (*a*) Large-scale streamwise velocity fluctuations u_l^+. The circles indicate the centre values of each segment. (*b*) Streamwise swirling strength λ_x^+. (*c*) Wall-normal swirling strength λ_y^+. The values multiplied by 10^{-2} indicate the inner-scaled r.m.s. of the swirling strength computed in each segment. Blue and red colours represent the signals for $u_l < 0$ and $u_l > 0$, respectively.

Note that λ_z is the spanwise wavelength. In the present study, the root mean square (r.m.s.) of λ_x and λ_y was conditionally sampled in terms of the strength of u_l to examine the modulation of the vortical structures. The conditional sampling method of Ganapathisubramani *et al.* (2012), which utilized a time series of hot-wire data, was extended to the swirling strength in the physical domain using the present dataset obtained from a DNS of TBL. The procedure used for the conditional sampling is summarized as follows:

(i) A long-wavelength-pass filter was applied to isolate the large scales of the streamwise velocity fluctuations (u_l), the spanwise wavelength of which exceeded 0.5δ (figure 3*a*).

(ii) The fluctuating signals were separated into individual segments of length 0.5δ (vertical dashed lines in figure 3).

(iii) The r.m.s. of the signals was computed at each segment (the values are inserted in each segment of figure 3), and the corresponding value of u_l in a segment was chosen as the centre value of each segment (circles in figure 3*a*).

Figure 3 presents a sample signal u_l^+ for λ_x and λ_y at $y^+ = 14.5$. Red and blue colours represent the velocity fluctuations with the representative large-scale fluctuations of $u_l > 0$ and $u_l < 0$, respectively. The signal of λ_x fluctuated significantly for the positive u_l. Similarly, the wall-normal swirling strength was amplified under the positive u_l compared to that under the negative u_l. A comparison of the r.m.s. values of each segment revealed that the amplitudes of λ_x and λ_y under the negative-u_l event were significantly lower than those measured under the positive-u_l event. Similar to the AM of u_s, the amplitudes of the swirling strengths were attenuated for $u_l < 0$ and amplified for $u_l > 0$ in the near-wall region. This observation was further explored statistically by computing the r.m.s. of the swirling strength over a range of wall-normal positions, as described in the following section.

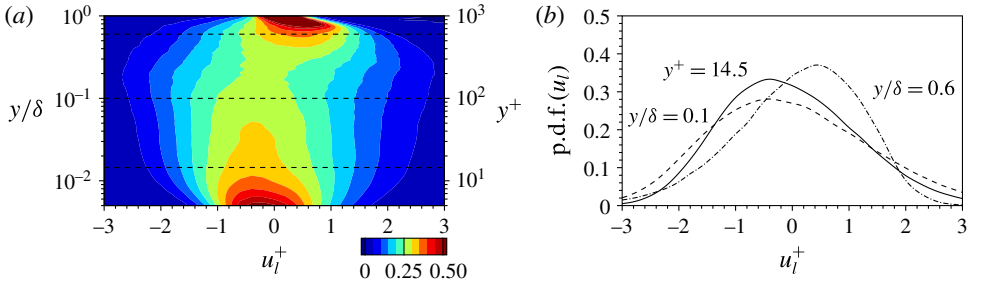

FIGURE 4. (Colour online) (*a*) The p.d.f. of the large-scale streamwise velocity fluctuations across the wall-normal direction. (*b*) The p.d.f. of the large-scale streamwise velocity fluctuations at $y^+ = 14.5$, $0.1\delta^+$ and $0.6\delta^+$ denoted by the dashed lines in (*a*).

4. Amplitude modulation of the vortical motions

We first examined the probability distribution of u_l across the wall-normal direction. The probability density function (p.d.f.) of u_l was defined as

$$\text{p.d.f.}(u_l) = \frac{N[u_l(y)]}{\int N[u_l(y)]\,\mathrm{d}u_l}, \tag{4.1}$$

where $N[u_l(y)]$ is the number of occurrences of u_l. The bin size of u_l^+ was set to 0.2. Figure 4(*a*) represents the p.d.f. of u_l across all wall-normal direction. The p.d.f. of u_l is relatively narrow near the wall, but widely distributed far from the wall. This result is similar to that obtained from the high Reynolds number experiments ($Re_\tau \approx 14\,000$) (Ganapathisubramani *et al.* 2012). The p.d.f. of u_l was the flattest at $y/\delta = 0.2$ (u_l frequently reached high magnitudes), consistent with the wall-normal position of the outer peak in the energy spectrum (figure 2). The p.d.f. of u_l was not symmetric about $u_l^+ = 0$. The distribution was biased toward the left below $y/\delta < 0.4$, representing that the negative u_l dominantly occurs in this range. This negatively biased distribution of u_l arose from the dominance of long negative-u regions in the log layer (Dennis & Nickels 2011; Hwang *et al.* 2016*b*). In addition, the low-speed regions were longer than their positive counterparts and, in particular, the long streaks carried significantly higher magnitude of u^+ that were 3 times the value of u_{rms}^+ in the log region (Hwang *et al.* 2016*b*). In figure 4(*b*), the p.d.f. of u_l at $y^+ = 14.5$ is also biased toward the left, indicating that the footprint of the large-scale negative-u structures was often present due to their dominance in the outer region.

The trend observed in figure 3 was explored by conditionally sampling the signals of the swirling strengths. The r.m.s. of the swirling strength (λ_x' and λ_y') could be computed as

$$\langle \lambda_x'(u_l, y)\rangle = \frac{\sum \lambda_x'(y)|_{u_l}}{N[u_l(y)]}, \quad \langle \lambda_y'(u_l, y)\rangle = \frac{\sum \lambda_y'(y)|_{u_l}}{N[u_l(y)]}. \tag{4.2a,b}$$

The conditionally averaged swirling strengths (4.2) represent the amplitudes of the vortical motions conditioned on the strength of u_l along the wall-normal direction. Note that the p.d.f. of u_l with a value lower than 10^{-5} was neglected to allow for statistical convergence. Figure 5(*ai*,*bi*) demonstrates the conditioned r.m.s. of the

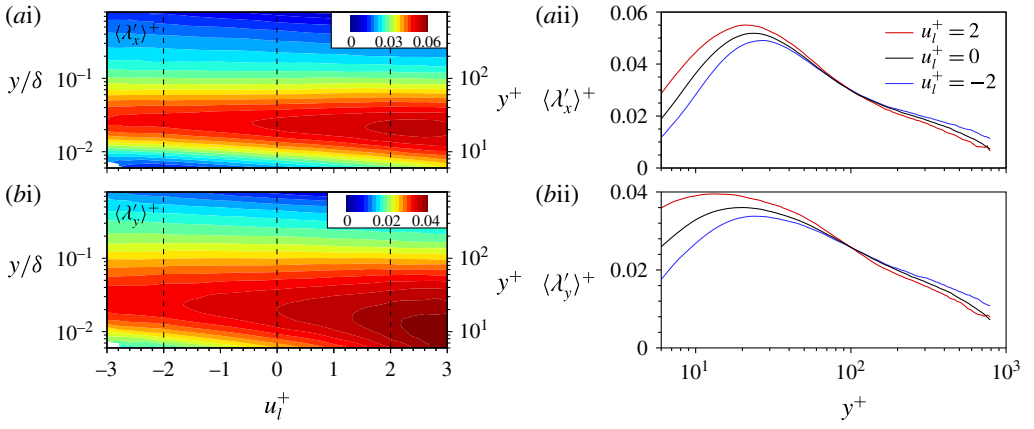

FIGURE 5. (Colour online) (i) The r.m.s. of the swirling strength (λ_i') conditioned on the large-scale fluctuations along the wall-normal direction. (ii) The r.m.s. of the swirling strength along the wall-normal direction for $u_l^+ = -2$, 0 and 2 (vertical dashed lines in *a*i,*b*i); (*a*) streamwise swirling strength; (*b*) wall-normal swirling strength.

swirling strengths, $\langle\lambda_x'\rangle$ and $\langle\lambda_x'\rangle$. In the near-wall region, intense regions of $\langle\lambda_x'\rangle$ and $\langle\lambda_y'\rangle$ appeared for the positive-u_l event, and their magnitudes decreased with decreasing u_l. This result clearly indicated that the amplitude of the vortical structures depended on the strength of the large scales, even though the near-wall structures sustained the turbulence without the presence of large scales in a minimal channel (Jiménez & Pinelli 1999). As y increased, both $\langle\lambda_x'\rangle$ and $\langle\lambda_y'\rangle$ decreased, regardless of the strength of u_l, but the rate of decrease depended on u_l. Figure 5(*a*ii,*b*ii) illustrates the profiles of $\langle\lambda_x'\rangle$ and $\langle\lambda_y'\rangle$ at $u_l^+ = -2$, 0 and 2. The intensity of the swirling strengths for $u_l^+ = 2$ was higher than that for $u_l^+ = -2$ in the near-wall region. This trend was reversed further from the wall because the profile of $u_l^+ = 2$ dropped rapidly. Above $y^+ \approx 100$, the swirling strengths under the negative-u_l event exceeded those under the positive-u_l event.

To further examine an asymmetric influence of u_l on the swirling strengths, the relative difference of the streamwise component $\Delta\lambda_i'$ between $\langle\lambda_i'(u_l, y)\rangle$ and $\langle\lambda_i'(u_l = 0, y)\rangle$ was defined as

$$\Delta\lambda_i' = \frac{\langle\lambda_i'(u_l, y)\rangle - \langle\lambda_i'(u_l = 0, y)\rangle}{\langle\lambda_i'(u_l = 0, y)\rangle}, \tag{4.3}$$

where the subscript i denotes x and y. The small scales for $u_l = 0$ could be interpreted as locally unmodulated signals because the effects of the carrier signal (u_l^+) were negligible (Ganapathisubramani *et al.* 2012). The velocity fields conditioned on the weak u_l in the near-wall region appeared as near-wall streaks, whereas the velocity fields conditioned on the intense u_l depicted the large-scale feature (see § B.1). In this regard, the conditionally sampled λ_i for $u_l = 0$ represents the swirling strength under a weak influence of the large scales, i.e. vortical motions in the non-footprint region. This interpretation is further discussed in § B.2. Hence, the relative difference $\Delta\lambda_i'(u_l, y)$ indicates the degree of the AM effect relative to the unmodulated swirling strength as a function of u_l and y.

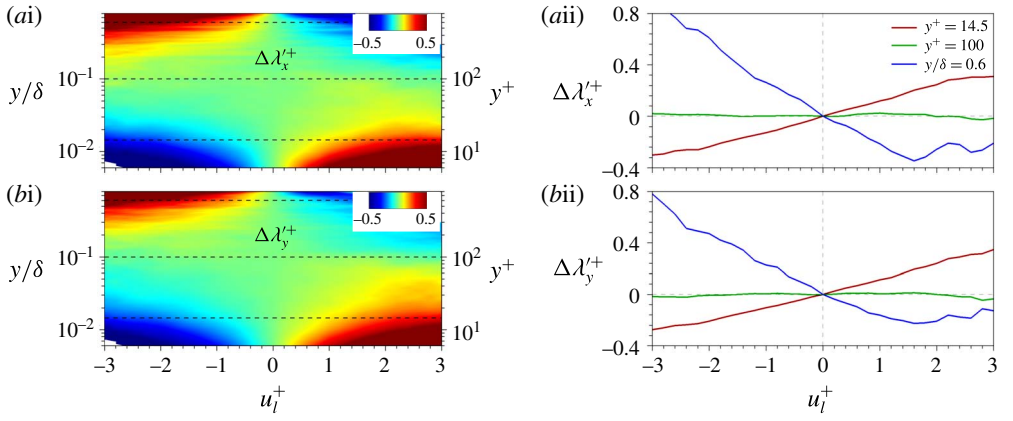

FIGURE 6. (Colour online) (i) Relative difference between $\langle\lambda_i'(u_l, y)\rangle$ and $\langle\lambda_i'(u_l = 0, y)\rangle$. (ii) Plot of the relative differences at three wall-normal locations; (*a*) streamwise swirling strength; (*b*) wall-normal swirling strength.

Figure 6(*a*i,*b*i) plots the contours of the relative difference $\Delta\lambda_i'(u_l, y)$. The negative values indicated a smaller magnitude (attenuation) of the small-scale variances compared to the unmodulated variance $u_l^+ = 0$. In general, the relative differences of the swirling strengths were not symmetric: the small-scale amplitudes increased for $u_l^+ > 0$ in the near-wall region, and this behaviour was reversed in the outer region. At $y^+ = 14.5$, the attenuation and amplification effects of the small-scale amplitudes varied within 40 % (red lines in figure 6*a*ii,*b*ii). Note that the relative difference of the streamwise velocity component in the high Reynolds number ($Re_\tau = 14\,150$) TBL (Ganapathisubramani *et al.* 2012) varied over a range similar to that observed in the present study ($Re_\tau = 1000$). The modulation effects were almost negligible at $y^+ = 100$, i.e. the relative differences were approximately zero, irrespective of u_l. In the outer region ($y/\delta = 0.6$), the amplification effect of the negative u_l was found to exceed the attenuation effect of the positive u_l. The asymmetric influence of the outer large scales on the cross-stream velocity components in the near-wall region was revealed through a joint probability analysis (Agostini & Leschziner 2014; Hwang *et al.* 2016*b*). The present results showed that the amplitudes of the swirling strength were modulated even in the outer region (attenuation for $u_l^+ > 0$ and amplification for $u_l^+ < 0$) in a manner analogous to that observed in the streamwise velocity component.

To summarize, the present results suggested that the streamwise and wall-normal swirling strengths associated with the quasi-streamwise vortices or the legs of hairpin-like vortices were influenced by the outer u_l. In the near-wall region, in particular, the strength of the vortical motions under the negative-u_l event was reduced, whereas the strength of the vortical motions under the positive-u_l event was enhanced. The modulation effect on the swirling strength was similar to that observed in the AM of the velocity fluctuations, indicating that the influence of u_l on the small-scale velocity fields was related to the modulation of the vortical structure. In the subsequent section, we examine the conditionally averaged velocity fields in order to investigate how the vortical motions were attenuated or amplified under the negative- and positive-u_l event by focusing on the relation between the modulated swirling strengths and their associated velocity fields.

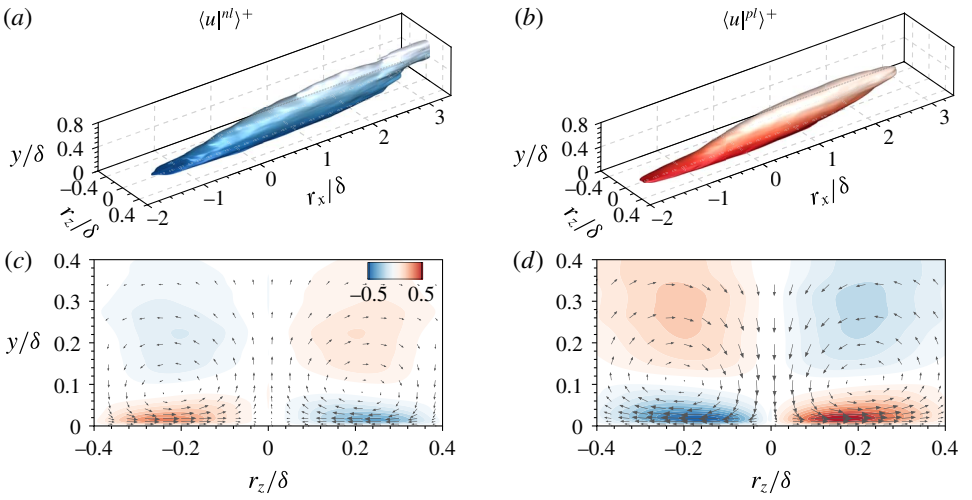

FIGURE 7. (Colour online) Conditional structures associated with the footprints of large-scale low- and high-speed structures at $y^+ = 14.5$. (*a*,*b*) Isosurfaces of streamwise velocity fluctuations $\langle u|^{nl}\rangle^+ = -0.5$ (blue) and $\langle u|^{pl}\rangle^+ = +0.5$ (red). Contours of spanwise velocity fluctuations (*c*) $\langle w|^{nl}\rangle^+$ and (*d*) $\langle w|^{pl}\rangle^+$ in the cross-stream plane ($r_x/\delta = 0$). The contour ranges from ± 0.05 to ± 0.5 with an increment of 0.05. Inserted vector represents the in-plane velocity components.

5. Conditional averaging analysis

5.1. *Velocity field associated with large-scale structures*

Before addressing the large-scale influence on the near-wall vortical structures, it is important to examine the flow field around the near wall u_l. The conditionally averaged velocities for the negative and positive u_l are defined as

$$\langle \boldsymbol{u}|^{nl}(r_x, y, r_z)\rangle = \langle \boldsymbol{u}(x + r_x, y, z + r_z)|u_l^+(x, y_{ref}, z) < -2\rangle, \tag{5.1}$$

$$\langle \boldsymbol{u}|^{pl}(r_x, y, r_z)\rangle = \langle \boldsymbol{u}(x + r_x, y, z + r_z)|u_l^+(x, y_{ref}, z) > +2\rangle. \tag{5.2}$$

Here, the superscript *nl* and *pl* denotes large-scale low- and high-speed conditions, respectively. The reference wall-normal position is $y^+ = 14.5$. Figure 7(*a*,*b*) illustrates isosurfaces of $\langle u|^{nl}\rangle$ and $\langle u|^{pl}\rangle$. Even though the reference wall-normal position is located at $y^+_{ref} = 14.5$, the conditional structures extended beyond the buffer layer (their height was approximately 0.6δ) as well as had their streamwise length over 5δ. On the contrary, the conditional structures for the weak strength of u_l ($|u_l^+(x, y_{ref}, z)| < 0.2$) showed that their streamwise lengths were approximately 1000 wall units and were enclosed within the buffer region (see § B.1). Therefore, the condition $|u_l^+(x, y_{ref}, z)| > 2$ could be considered as the footprint of the outer large-scale structures. In § 5.2, the near-wall vortical structures lying under the footprint of the large-scale structures was investigated based on this condition.

Figure 7(*c*,*d*) represents the cross-stream plane of the conditionally averaged field at $r_x/\delta = 0$. Conditional structures of both negative and positive u_l contained a pair of roll motions whose centres were located at $y/\delta = 0.1$; for the weak u_l^+ condition, the smaller circulations were observed and their centres were located at $y^+ = 30$ in figure 16. The flow fields associated with each structures have remarkably distinct features. For the negative u_l (figure 7*c*), the ejection event

occurred whereas the sweep event was observed in the conditional structure of the positive u_l (figure 7*d*). As a result of the opposite wall-normal motions (i.e. $v > 0$ and $v < 0$ for ejections and sweeps), each conditional structure induced opposite spanwise near-wall motions. Hwang *et al.* (2016*b*) described these features as the congregative and dispersive motions under the negative and positive u_l to distinguish the splatting and anti-splatting motions associated with the near-wall sweep and ejection events. In addition, the maximum $\langle w|^{pl}\rangle^+$ is 0.63 (1.2 times greater than the maximum $\langle w|^{nl}\rangle^+$), indicating that the strength of the dispersive motions induced by $u_l > 0$ were intense compared to the congregative motion. The congregative motion related to the outer ejections was reduced, because the spanwise motion under the large-scale circulation on both sides of the negative structure decreased as the flows came close to each other. On the other hand, the sweep of high-momentum fluid coming down to the wall involved a significant reduction of v and splatted on the wall, leading to the intense spanwise momentum. Therefore, this different magnitude of the spanwise motion arose from the nature of low- and high-speed structures, which were related to the ejection and sweep event, respectively. In § 5.2, the influence of large-scale structures on the near-wall vortical structures is examined by focusing on the near-wall spanwise motions induced by the outer large-scale structures.

5.2. *Near-wall vortical structures conditioned on the large-scale events*

The r.m.s. of the swirling strength conditioned on u_l (§ 4) demonstrated that the outer large scales not only influenced the small-scale velocity fluctuations but also the vortical structures. However, the relationship between the modulated velocity fluctuations and the modulated vortical structures was unclear and, thus an examination of the flow field around the swirling strength was necessary to reveal how the outer large-scale motions affected the vortical structures in the near-wall region. This section provides a physical explanation of this phenomenon by analysing the conditionally averaged velocity fields associated with the modulated vortical structures.

We first explored the spatial organization of the near-wall streamwise swirling strength (λ_x) associated with the quasi-streamwise vortices under the influence of the large-scale structures. The conditionally averaged λ_x under the footprints of the negative and positive u_l was defined as

$$\langle \lambda_x|^{nl}(r_x, y, r_z)\rangle = \langle \lambda_x(x + r_x, y, z + r_z)|u_l^+(x, y_{ref}, z) < -2\rangle, \tag{5.3}$$

$$\langle \lambda_x|^{pl}(r_x, y, r_z)\rangle = \langle \lambda_x(x + r_x, y, z + r_z)|u_l^+(x, y_{ref}, z) > +2\rangle. \tag{5.4}$$

Note that positive and negative streamwise vorticity fluctuations (ω_x) were equally probable in the near-wall region because the quasi-streamwise vortices were dominant in this region; i.e. the streamwise vortical structures with negative ω_x were the symmetric counterparts to the structures with positive ω_x (Jeong *et al.* 1997). In the present study, we focused our analysis only on positive $\lambda_x = \lambda_{ci,x}\omega_x/|\omega_x|$.

The conditional structures of the streamwise vortical structures are shown in figure 8. Note that the conditional structure for the weak-u_l event ($\langle \lambda_x|^{ss}\rangle$) was computed for comparison with figure 8 in § B.2 (figure 17*a*). The streamwise extents and diameters of both of the structures ($\langle \lambda_x|^{nl}\rangle$ and $\langle \lambda_x|^{pl}\rangle$) were approximately 200 and 30 wall units, respectively, consistent with the work of Jeong *et al.* (1997) who educed the streamwise vortical structures in the near-wall region without applying large-scale conditions. By comparing $\langle \lambda_x|^{nl}\rangle$ and $\langle \lambda_x|^{pl}\rangle$ precisely, however, the

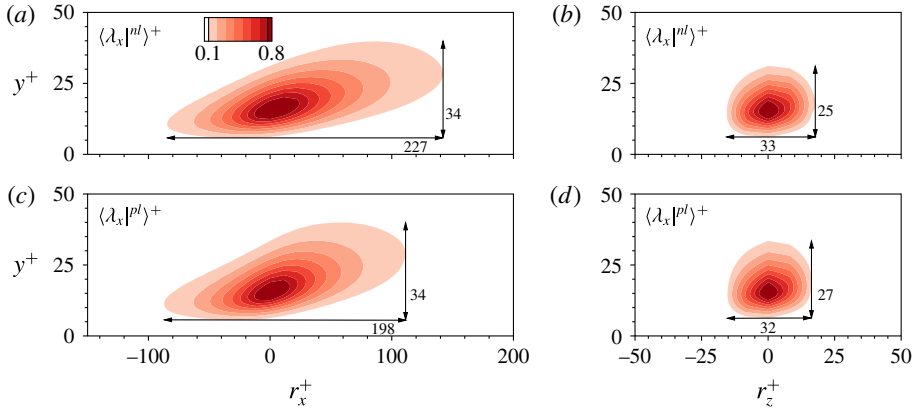

FIGURE 8. (Colour online) Conditional structures associated with the streamwise swirling strength influenced by the outer large-scale low- and high-speed structures, $\langle\lambda_x|^{nl}\rangle^+$ and $\langle\lambda_x|^{pl}\rangle^+$: (*a*,*c*) *x*–*y* plane ($r_z^+ = 0$); (*b*,*d*) *y*–*z* plane ($r_x^+ = 0$). The contours represent the conditioned swirling strength normalized by its maximum value. The contours range from 0.1 to 0.8 with an increment of 0.1.

conditional structures were found to have distinct features that depended on the large-scale condition. The conditional structure of $\langle\lambda_x|^{pl}\rangle$ was slightly longer than that of $\langle\lambda_x|^{nl}\rangle$, whereas the height of both structures is 34 wall units (figure 8*a*,*c*). As a result, the former was steeply inclined along an angle of 9.7° compared to the latter, 8.5° (cf. the inclination angle of $\langle\lambda_x|^{ss}\rangle$ was 9.1° in figure 17*a*). The maximum values of $\langle\lambda_x\rangle^+$ for the positive- and negative-u_l conditions were 0.07 and 0.05, respectively. The streamwise vortices in the near-wall region under the positive-u_l event were intense, consistent with the results observed in the conditioned r.m.s. value $\langle\lambda_x'\rangle$ (figures 5); the maximum value of $\langle\lambda_x'\rangle^2$ for $u_l^+ = 2$ was approximately 1.3 times the value for $u_l^+ = -2$. Thus, the conditional structures shown in figure 8 clearly captured the quasi-streamwise vortices and their dependence on the strength of u_l observed in § 4.

In figure 8(*b*,*d*), the diameter of the conditioned vortical structures was approximately 30 wall units in the negative- and positive-u_l events, which was consistent with Fiscaletti, Ganapathisubramani & Elsinga (2015) that the diameter of the vortical structures was unchanged in a turbulent jet. However, the streamwise extent of $\langle\lambda_x|^{nl}\rangle$ was approximately 1.2 times longer than that of $\langle\lambda_x|^{pl}\rangle$ (figure 8*a*,*c*). Since the intense vortices lay within the footprint of the positive-u_l structures (or embedded within the high-speed region), these structures could convect with a higher velocity than the mean streamwise velocity. The differences of the streamwise extent of vortices between the negative- and positive-u_l conditions were similar to the differences between the vortices with the no-slip and with the shear-stress boundary condition (see figures 7 and 8 in Chung, Monty & Ooi (2014)). Owing to the high-speed region close to the wall, the streamwise vortices (legs of the hairpin-like vortices) could slide along the wall. In other words, the region of the positive-u_l footprint, which was located slightly above the wall (viscous sublayer), acted as a slip wall. On the other hand, the vortices within the negative-u_l footprint were anchored to the wall due to the region of the low-speed flow, leading to the elongation of vortices with a shallow angle, as compared to the vortices under the influence of the positive u_l.

In addition, Toh & Itano (2005) found that the outer large-scale negative-u structures were generated by the collective behaviour of near-wall structures. As time elapsed, a

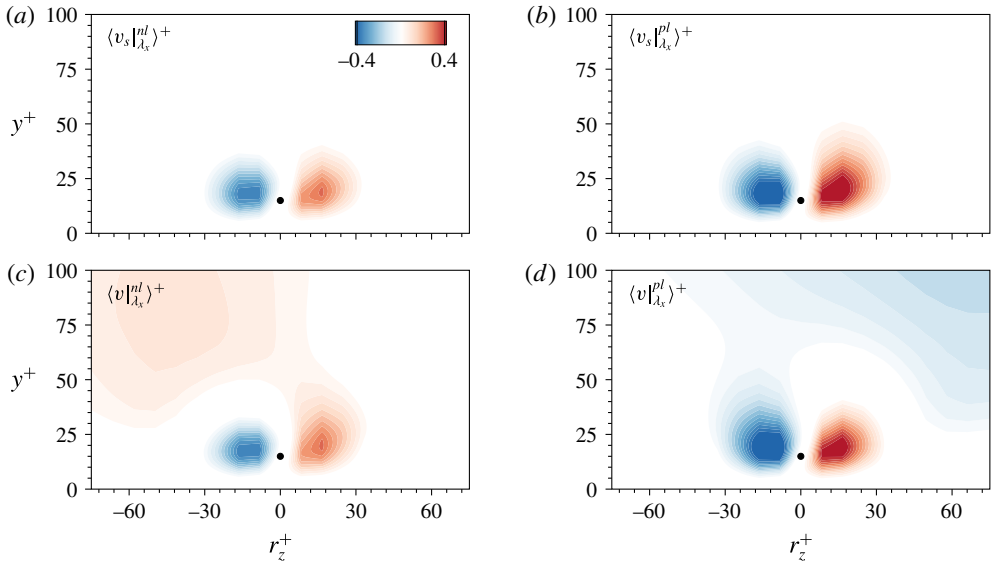

FIGURE 9. (Colour online) (*a*,*b*) Conditionally averaged small-scale wall-normal velocity fluctuations under the negative and positive-u_l conditions ($\langle v_s|^{nl}_{\lambda_x}\rangle$ and $\langle v_s|^{pl}_{\lambda_x}\rangle$) in the cross-stream plane ($r_x^+ = 0$). (*c*,*d*) Conditionally averaged total wall-normal velocity fluctuations under the negative and positive-u_l conditions ($\langle v|^{nl}_{\lambda_x}\rangle$ and $\langle v|^{pl}_{\lambda_x}\rangle$) in the cross-stream plane ($r_x^+ = 0$). The black dot indicates the reference position, $y^+_{ref} = 14.5$. The contour levels are $\pm(0.1 : 0.025 : 0.4)$.

group of the minima of u in the low-speed region gathered under the outer low-speed structures, whereas the minima in the high-speed region emerged as 'scattered points'. Given that the group of the local minima lived long under the low-speed region while not under the high-speed region, the difference in the streamwise length between the modulated vortical structures (figures 8) might be related with the scattered points. The vortical structures whose streamwise length was relatively long could survive for a longer time than the shorter ones. The near-wall vortices moved along the wall with a stretching motion, which led to a decrease in the gap between the legs of hairpin-like vortex (or quasi-streamwise vortex); the length and width decreased while the height increased as time goes by. Accordingly, the relatively short streamwise vortex with a steep inclination angle could be regarded as a mature vortex, i.e. such a vortex would dissipate soon; the relatively short vortices with a steep inclination angle under the footprint of high-speed regions (figure 8) were related to the short-lived branches of the local minima under a separation region.

The differences in λ_x obtained under the negative and positive u_l were further examined by educing the flow field around the modulated λ_x, which provided a connection to the amplified or attenuated small-scale velocity fluctuations ($\boldsymbol{u}_s$). The conditionally averaged $\boldsymbol{u}_s$ associated with the modulated λ_x under the footprints of the negative and positive u_l were defined as

$$\langle \boldsymbol{u}_s|^{nl}_{\lambda_x}(r_x, y, r_z)\rangle = \langle \boldsymbol{u}_s(x + r_x, y, z + r_z)|\lambda_x(x, y_{ref}, z) > 0 \text{ and } u_l^+(x, y_{ref}, z) < -2\rangle, \quad (5.5)$$

$$\langle \boldsymbol{u}_s|^{pl}_{\lambda_x}(r_x, y, r_z)\rangle = \langle \boldsymbol{u}_s(x + r_x, y, z + r_z)|\lambda_x(x, y_{ref}, z) > 0 \text{ and } u_l^+(x, y_{ref}, z) > +2\rangle. \quad (5.6)$$

Figures 9(*a*,*b*) and 10(*a*,*b*) show the educed cross-stream components of the small scales ($\langle v_s|_{\lambda_x}\rangle$ and $\langle w_s|_{\lambda_x}\rangle$), which contributed to the streamwise swirling motions, in

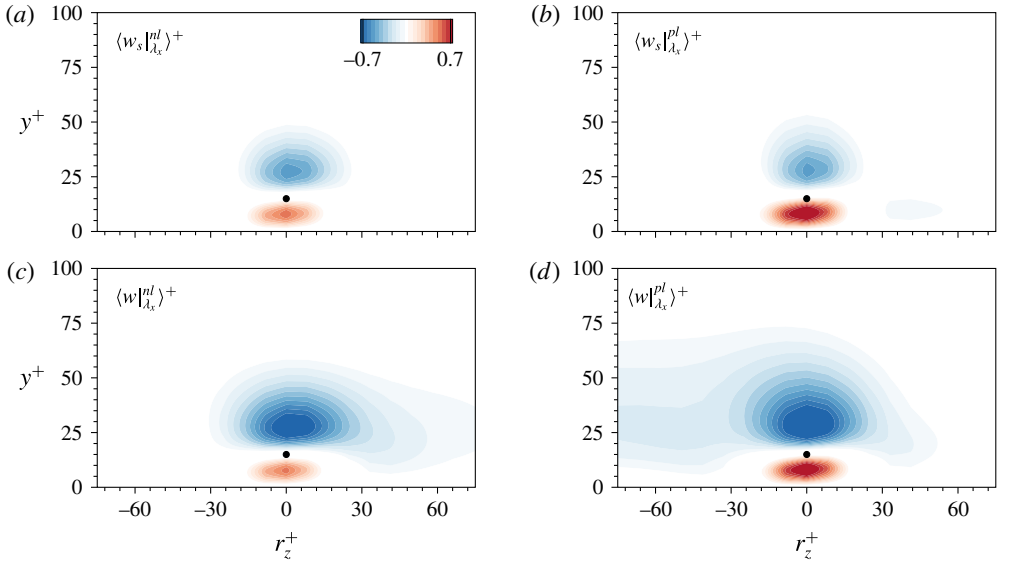

FIGURE 10. (Colour online) (*a*,*b*) Conditionally averaged small-scale spanwise velocity fluctuations under the negative and positive-u_l conditions ($\langle w_s|^{nl}_{\lambda_x}\rangle$ and $\langle w_s|^{pl}_{\lambda_x}\rangle$) in the cross-stream plane ($r_x^+ = 0$). (*c*,*d*) Conditionally averaged total spanwise velocity fluctuations under the negative and positive-u_l conditions ($\langle w|^{nl}_{\lambda_x}\rangle$ and $\langle w|^{pl}_{\lambda_x}\rangle$) in the cross-stream plane ($r_x^+ = 0$). The black dot indicates the reference position, $y^+_{ref} = 14.5$. The contour levels are $\pm(0.2 : 0.05 : 0.7)$.

the y–z plan ($r_x^+ = 0$). The flow fields of both the negative- and positive-u_l events indicated the presence of a counter-clockwise swirling motion around the reference position (cf. the vectors in figures 11 and 12). However, the magnitudes of both $\langle v_s|_{\lambda_x}\rangle$ and $\langle w_s|_{\lambda_x}\rangle$ depended on the large-scale event.

For the small-scale wall-normal components (figure 9*a*,*b*), the positive and negative regions (upwash and downwash motions) were intense under the positive-u_l event compared to the negative-u_l event; the maximum values of $\langle v_s|^{pl}_{\lambda_x}\rangle^+$ and $\langle v_s|^{nl}_{\lambda_x}\rangle^+$ were 0.5 and 0.4, respectively. For the small-scale spanwise components (figure 10*a*,*b*), the negative- and positive-w_s region was located above and below the centre of the vortex. In particular, the positive-w_s region was noticeably strengthened under the positive-u_l event, whereas the negative-w_s region had comparable magnitudes under the negative- and positive-u_l event (compare figure 10*a* with 10*b*); the minimum value was -0.6 for both events, while the maximum values of $\langle w_s|^{pl}_{\lambda_x}\rangle^+$ and $\langle w_s|^{nl}_{\lambda_x}\rangle^+$ were 0.9 and 0.6, respectively. These observations indicated that the amplitude attenuation and amplification of the small-scale cross-stream components were attributed to the dependence of the streamwise vortical motions on the u_l event.

A noteworthy feature of figure 10(*a*,*b*) is that only the positive-w_s region ($y < y_{ref}$) was strengthened under the positive-u_l event. In contrast to the modulation of v_s (i.e. amplification of v_s on both sides of the swirling motions in figure 9*b*), this behaviour indicated that the large-scale high-speed structure influenced the amplitude of w_s below the centre of the vortical motions. This phenomenon was further investigated by conditionally averaging the total velocity fluctuations ($\boldsymbol{u}$), which possessed the large-sale components. The educed cross-stream components of the total fluctuations ($\langle v|_{\lambda_x}\rangle$ and $\langle w|_{\lambda_x}\rangle$) are presented in figures 9(*c*,*d*) and 10(*c*,*d*). The cross-stream

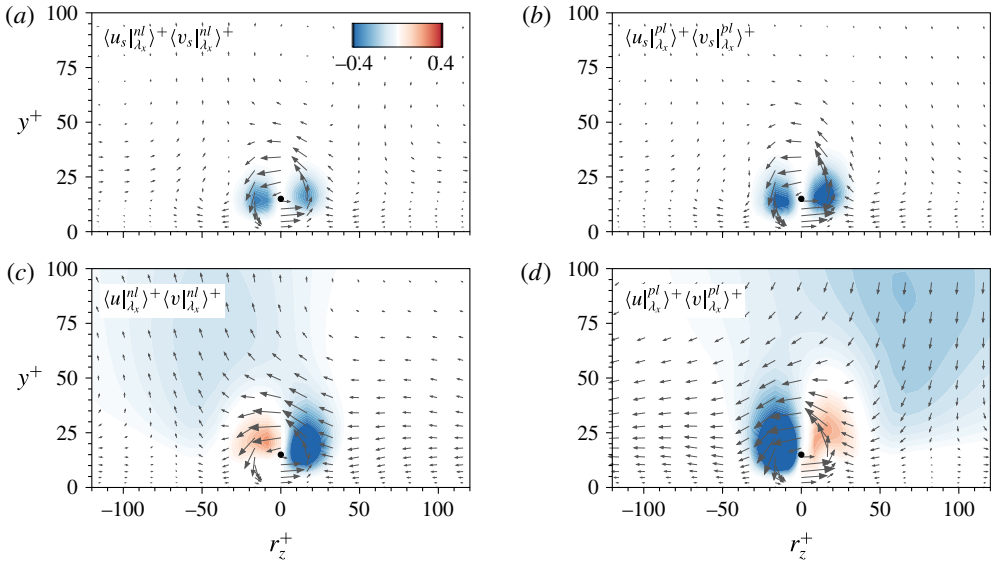

FIGURE 11. (Colour online) Contours of coherent Reynolds stresses in the cross-stream plane ($r_x = 0$): (*a*) $\langle u_s|^{nl}_{\lambda_x}\rangle\langle v_s|^{nl}_{\lambda_x}\rangle$; (*b*) $\langle u_s|^{pl}_{\lambda_x}\rangle\langle v_s|^{pl}_{\lambda_x}\rangle$; (*c*) $\langle u|^{nl}_{\lambda_x}\rangle\langle v|^{nl}_{\lambda_x}\rangle$; (*d*) $\langle u|^{pl}_{\lambda_x}\rangle\langle v|^{pl}_{\lambda_x}\rangle$. Vectors indicate the in-plane velocity components of the corresponding event. The black dot indicates the reference position, $y^+_{ref} = 14.5$. The contour levels are $\pm(0.05 : 0.025 : 0.4)$.

components clearly differed from the educed small scales (compare figures 9*a*,*b* and 10*a*,*b* respectively with figures 9*c*,*d* and 10*c*,*d*) due to the presence of large scales. Note that the educed total velocity fluctuations for the weak u_l (figure 17*b*) represent an absence of large-scale circulations, revealing that the large-scale features described here were important for explaining the differences between the flow fields obtained under the negative and positive u_l event.

In figure 9(*c*,*d*), the wall-normal component included wide regions of positive and negative v beyond the buffer region, indicative of the upwash and downwash motions associated with the outer ejection and sweep events induced by large-scale structures. Likewise, congregative and dispersive motions, which were represented by the intense negative-w regions above y_{ref}, were observed in the spanwise component for the negative- and positive-u_l event, respectively (figure 10*c*,*d*). The magnitudes of the positive w ($y < y_{ref}$) in figure 10(*c*,*d*) were similar to the positive w_s in figure 10(*a*,*b*); the maximum values of $\langle w|^{pl}_{\lambda_x}\rangle^+$ and $\langle w|^{nl}_{\lambda_x}\rangle^+$ were 0.9 and 0.6, respectively, consistent with those of $\langle w_s|^{pl}_{\lambda_x}\rangle^+$ and $\langle w_s|^{nl}_{\lambda_x}\rangle^+$. In other words, the large-scale component was not superimposed on the spanwise velocity fluctuations below the centre of the modulated vortical structures, whereas the large-scale spanwise motions appeared above the centre of the modulated vortical structures. Along the spanwise direction, in particular, the negative-w region of $\langle w|^{pl}_{\lambda_x}\rangle^+$ prevailed with a greater magnitude compared to that of $\langle w|^{nl}_{\lambda_x}\rangle^+$. This result was reminiscent of the strong spanwise motions within the footprint of positive u_l (cf. figure 7*d*). The near-wall spanwise motions induced by positive-u_l structures strengthened the opposite spanwise motion (positive-w_s region in figure 10*b*) below the centre of the streamwise vortical structures, whereas the small-scale spanwise component was relatively weakened under the negative-u_l event due to the relatively weak spanwise motions.

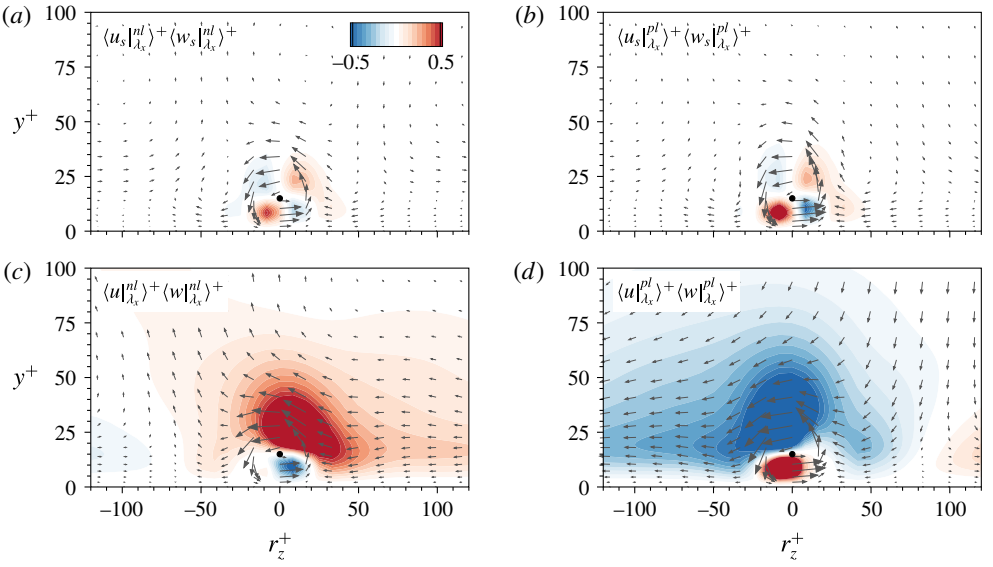

FIGURE 12. (Colour online) Contours of coherent Reynolds stresses in the cross-stream plane ($r_x = 0$): (*a*) $\langle u_s|^{nl}_{\lambda_x}\rangle\langle w_s|^{nl}_{\lambda_x}\rangle$; (*b*) $\langle u_s|^{pl}_{\lambda_x}\rangle\langle w_s|^{pl}_{\lambda_x}\rangle$; (*c*) $\langle u|^{nl}_{\lambda_x}\rangle\langle w|^{nl}_{\lambda_x}\rangle$; (*d*) $\langle u|^{pl}_{\lambda_x}\rangle\langle w|^{pl}_{\lambda_x}\rangle$. Vectors indicate the in-plane velocity components of the corresponding event. The black dot indicates the reference position, $y^+_{ref} = 14.5$. The contour levels are $\pm(0.05 : 0.05 : 0.5)$.

Figures 11(*a*,*b*) and 12(*a*,*b*) present a wide view of the Reynolds stresses associated with the small-scale components. Figure 11(*a*,*b*) indicated that intense regions of negative $\langle u_s|_{\lambda_x}\rangle\langle v_s|_{\lambda_x}\rangle$ appeared on both sides of the vortical structure. The magnitude of these regions, in particular, was noticeably greater for the positive-u_l event; the minimum values of $\langle u_s|^{nl}_{\lambda_x}\rangle\langle v_s|^{nl}_{\lambda_x}\rangle$ and $\langle u_s|^{pl}_{\lambda_x}\rangle\langle v_s|^{pl}_{\lambda_x}\rangle$ were -0.37 and -0.59, respectively. These results revealed that the amplification of the small-scale velocity components under the footprints of the positive-u_l structures enhanced vertical momentum transport. Furthermore, the magnitudes of $\langle u_s|^{pl}_{\lambda_x}\rangle\langle w_s|^{pl}_{\lambda_x}\rangle$ below the centre of the vortex exceeded those of $\langle u_s|^{nl}_{\lambda_x}\rangle\langle w_s|^{nl}_{\lambda_x}\rangle$ (figure 12*a*,*b*), indicating that the spanwise transport of the streamwise momentum was also dominant for the positive-u_l event. The intense regions of $\langle u_s|^{pl}_{\lambda_x}\rangle\langle w_s|^{pl}_{\lambda_x}\rangle$ arose from the amplification of the positive w_s as observed in figure 10(*b*).

Figure 11(*c*,*d*) displays the cross-stream plane of $\langle u|^{nl}_{\lambda_x}\rangle\langle v|^{nl}_{\lambda_x}\rangle$ and $\langle u|^{pl}_{\lambda_x}\rangle\langle v|^{pl}_{\lambda_x}\rangle$. The outer ejection and sweep motions were observed in contrast to figure 11(*a*,*b*). Note that the outer ejection and sweep motions were not observed under the weak-u_l condition (see figure 17*b*). Figure 12(*c*,*d*) shows the large spanwise extent of the positive and negative regions of $\langle u|_{\lambda_x}\rangle\langle w|_{\lambda_x}\rangle$ above the reference position. Given the spanwise direction of the inserted vectors (negative w for the negative- and positive-u_l conditions), the modulated vortical structures under the influence of negative or positive u_l were embedded within the streamwise velocity, which was lower or higher than the mean streamwise velocity. In addition, the large spanwise extent of the positive and negative regions indicated the presence of the congregative and dispersive motions under the footprints of negative and positive u_l, respectively. The strong spanwise motions for the positive-u_l event produced a larger maximum magnitude of $\langle u|^{pl}_{\lambda_x}\rangle\langle w|^{pl}_{\lambda_x}\rangle^+$ ($\approx$1.6) compared to that of $\langle u|^{nl}_{\lambda_x}\rangle\langle w|^{nl}_{\lambda_x}\rangle^+$ ($\approx$1.3). This result

demonstrated that the modulated vortical motions lay within the outer large-scale circulations, and that the vertical and lateral momentum transports were enhanced or diminished in connection with the AM of the small-scale velocity fluctuations. Note that the flow fields associated with the modulated λ_y showed similar results to λ_x (not shown here), indicating that the intense spanwise motions under the positive-u_l event contributed to the amplification of the velocity fields around the modulated λ_y.

6. Influence of large-scale motions on the skin-friction coefficient

In this section, we analyse the contribution of the modulated vortical motions to the skin friction. Since the near-wall vortical structures were responsible for the Reynolds shear stress (Robinson 1991) and the Reynolds shear stress was directly related to the skin friction (Fukagata, Iwamoto & Kasagi 2002), the amplification and attenuation of the swirling motions, and also their associated velocity fields (§ 5) would have an influence on the local skin-friction coefficient (C_f). In order to quantify the contribution of the modulated vortical motions on C_f, we used a new decomposition method for C_f as suggested by Yoon *et al.* (2016*a*). The details of the derivation procedure are described in Yoon *et al.* (2016*a*). Using this method, C_f could be decomposed into five parts,

$$C_f = \underbrace{\int_0^1 2\left(1-\frac{y}{\delta}\right)\frac{\langle v\omega_z\rangle}{U_\infty^2/\delta}\,\mathrm{d}\left(\frac{y}{\delta}\right)}_{C_{f1}} + \underbrace{\int_0^1 2\left(1-\frac{y}{\delta}\right)\frac{\langle -w\omega_y\rangle}{U_\infty^2/\delta}\,\mathrm{d}\left(\frac{y}{\delta}\right)}_{C_{f2}}$$
$$+ \underbrace{\frac{\nu\delta}{U_\infty^2}\left.\frac{\partial\Omega_z}{\partial y}\right|_{y=0}}_{C_{f3}} + \underbrace{\frac{\nu}{U_\infty^2}\int_0^1 -2\Omega_z\,\mathrm{d}\left(\frac{y}{\delta}\right)}_{C_{f4}} + \underbrace{\int_0^1\left(1-\frac{y}{\delta}\right)^2\langle I_x\rangle\frac{\delta^2}{U_\infty^2}\,\mathrm{d}\left(\frac{y}{\delta}\right)}_{C_{f5}}, \quad (6.1)$$

$$\langle I_x\rangle = \frac{\partial}{\partial x}(U\Omega_z + \langle u\omega_z\rangle - \langle w\omega_x\rangle) + \frac{\partial}{\partial y}(V\Omega_z) - \nu\frac{\partial^2\Omega_z}{\partial x^2}. \quad (6.2)$$

The first and second terms (C_{f1} and C_{f2}) represent the contributions of the velocity–vorticity correlations $\langle v\omega_z\rangle$ and $\langle w\omega_y\rangle$. The third and fourth terms (C_{f3} and C_{f4}) indicate the contributions of the molecular diffusion at the wall and the molecular transfer due to the mean vorticity, respectively. The last term (C_{f5}) is the contribution of a spatial development term $\langle I_x\rangle$ (6.2). In the present study, we focus on the second term (C_{f2}) which was the dominant contribution to C_f. Furthermore, the velocity–vorticity correlation $\langle -w\omega_y\rangle$ was associated with the change-of-scale effect related to the vortex-stretching force. Using a mixing length representation, $\langle -w\omega_y\rangle$ is scaled as $u^*(\partial U/\partial y)(\partial l/\partial y)$, where u^* is the characteristic velocity and l is the length scale. $\langle -w\omega_y\rangle$ can be interpreted as a body force related to the change of scale of eddies ($\partial l/\partial y$) with the vorticity of $O(\partial U/\partial y)$ (Tennekes & Lumley 1972). The profile of $\langle -w\omega_y\rangle$ had a positive peak in the near-wall region due to either (i) $w>0$ and $\omega_y<0$ or (ii) $w<0$ and $\omega_y>0$. Physically, a positive value of $\langle -w\omega_y\rangle$ was consistent with the two legs of hairpin-like vortices (or streamwise vortices) moving close to one another, and then stretching as they advected from the wall. In addition, $\langle -w\omega_y\rangle$ was closely related to the AM (change of length scale) of the small scales by the large-scale motions (Chin *et al.* 2014; Hwang, Lee & Sung 2016*a*). Hence, the contribution of the modulated vortical motions to C_f was directly quantified by computing the C_{f2} term.

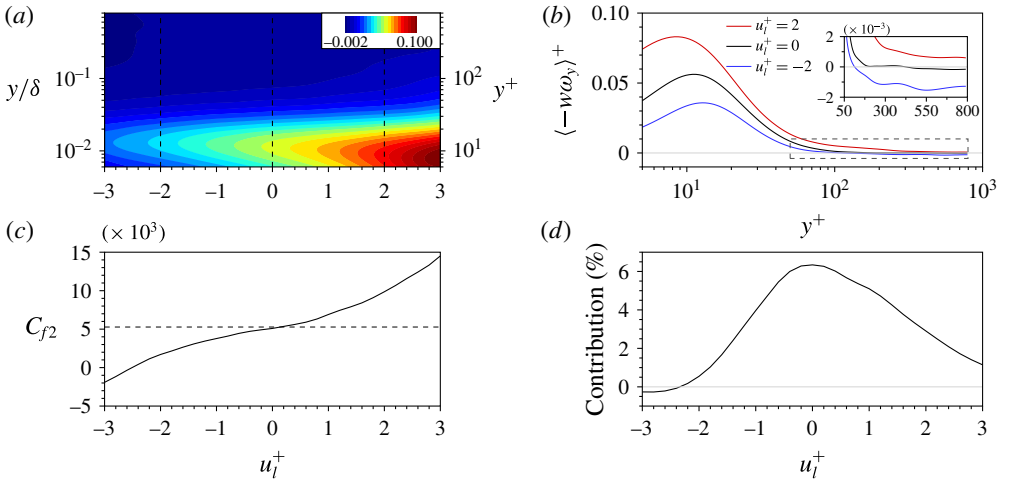

FIGURE 13. (Colour online) (*a*) Correlation between the spanwise velocity fluctuations and the wall-normal velocity fluctuations conditioned on the large-scale fluctuations along the wall-normal direction, $\langle -w\omega_y(u_l, y)\rangle^+$. (*b*) Profiles of $\langle -w\omega_y(u_l, y)\rangle^+$ along the wall-normal direction for $u_l^+ = -2$, 0 and 2. (*c*) Dependence of the skin friction induced by $\langle -w\omega_y(u_l, y)\rangle$ on the large-scale fluctuations, $\langle C_{f2}(u_l)\rangle$. The dashed lines indicate C_{f2} in (6.1). (*d*) Contribution of $\langle C_{f2}(u_l)\rangle$ to C_{f2}, $C_{f2}^{con}(u_l)$.

We first evaluated the velocity–vorticity correlation between the spanwise velocity and wall-normal vorticity fluctuations ($\langle -w\omega_y\rangle$) conditioned on the strength of u_l similar to (4.2). The correlation can be computed as

$$\langle -w\omega_y(u_l, y)\rangle = \frac{\sum w(y)\omega_y(y)|_{u_l}}{N[u_l(y)]}. \tag{6.3}$$

Figure 13(*a*) shows the contour of $\langle -w\omega_y(u_l, y)\rangle^+$. In the near-wall region, intense regions appeared for the positive u_l and $\langle -w\omega_y(u_l, y)\rangle^+$ decreased with decreasing u_l. The wall-normal vortical motion within the footprint of u_l and its associated spanwise velocity were modulated by u_l (§ 5), which, in turn, contributed to the dependence of $\langle -w\omega_y\rangle$ on the strength of u_l. Unlike with λ_x and λ_y (figure 5), $\langle -w\omega_y(u_l, y)\rangle^+$ decreased rapidly beyond $y^+ \approx 50$, regardless of u_l. Figure 13(*b*) shows the profiles of $\langle -w\omega_y(u_l, y)\rangle^+$ for $u_l^+ = -2$, 0 and 2. The profiles reached a distinct peak at $y^+ \approx 12$ and decayed close to zero as y increased. The inset in figure 13(*b*) plots a zoomed-in view of the region above $y^+ \approx 50$. The profile of $\langle -w\omega_y(u_l, y)\rangle^+$ for $u_l^+ = -2$ crossed zero at $y^+ \approx 100$ and attained a constant negative value, indicating that the vortex stretching in this region negatively contributed to C_{f2}. In other words, the value of C_{f2} in this region was negative as a result of integrating $\langle -w\omega_y\rangle$ from $y^+ = 100$ to $y^+ = \delta^+$, which was attributed to a reduction in the skin friction. For $u_l^+ = 2$, by contrast, the profile of $\langle -w\omega_y\rangle$ was positive and reached a higher magnitude along the wall-normal direction; thus, the vortex stretching (amplified vortical motions) under the influence of positive u_l enhanced C_f.

Next, the frictional drag induced by the modulated $\langle -w\omega_y\rangle$ was examined by obtaining the second term in (6.1) as a function of u_l,

$$\langle C_{f2}(u_l)\rangle = \int_0^1 2\left(1 - \frac{y}{\delta}\right)\frac{\langle -w\omega_y(u_l, y)\rangle}{U_\infty^2/\delta}\,\mathrm{d}\left(\frac{y}{\delta}\right). \tag{6.4}$$

In figure 13(*c*), the skin friction induced by the vortex stretching effect (or change-of-scale effect) varied with the strength of u_l, indicating that the modulation of vortical motions was directly attributed to the dependence of the local skin friction on the large-scale structures. Here, the horizontal line indicates C_{f2} in (6.1). The value of $\langle C_{f2}(u_l)\rangle$ for the positive u_l exceeded the value of C_{f2}, whereas this trend was reversed for the negative u_l. The amplified vortical motions within the footprint of positive u_l induced the high skin friction, more than 3 times greater than the mean C_{f2}. Conversely, the vortical motions, which were attenuated within the footprint of the negative u_l, contributed to the low skin friction. This observation was connected to the relationship between the footprints of the large-scale low-speed structure and the large-scale low skin-friction event (Hutchins *et al.* 2011), as well as with the locally low or high Re_τ within the negative- or positive-u_l footprints (Chernyshenko *et al.* 2012; Ganapathisubramani *et al.* 2012).

Given that the p.d.f. of u_l was antisymmetric with respect to $u_l^+ = 0$ (figure 4), we considered the contribution of $\langle C_{f2}(u_l)\rangle$ to C_{f2}. The contribution of $\langle C_{f2}(u_l)\rangle$ (C_{f2}^{con}) could be computed according to

$$C_{f2}^{con}(u_l) = \frac{1}{C_{f2}} \int_0^1 2\left(1 - \frac{y}{\delta}\right) \frac{\langle -w\omega_y(u_l, y)\rangle}{U_\infty^2/\delta} C(u_l, y)\, \mathrm{d}\left(\frac{y}{\delta}\right), \tag{6.5}$$

$$C(u_l, y) = \frac{N[u_l(y)]}{\sum N[u_l(y)]}, \tag{6.6}$$

$$\sum_{u_l=-\infty}^{\infty} C_{f2}^{con}(u_l) = \frac{C_{f2}}{C_{f2}} = 1. \tag{6.7}$$

As shown in figure 13(*d*), the plot of $C_{f2}^{con}(u_l)$ was not symmetric with respect to $u_l^+ = 0$. A peak appeared at $u_l^+ = 0$ due to the dominance of the weak-u_l event (i.e. a peak in the p.d.f. of u_l was located in the vicinity of $u_l^+ \approx 0$ in figure 4). The contribution of $u_l < 0$ was quite small compared to that of $u_l > 0$. A negative contribution was observed in the range $u_l^+ < -2.3$ because $\langle -w\omega_y\rangle < 0$ in the outer region became dominant compared to $\langle -w\omega_y\rangle > 0$ in the near-wall region. As a result, the cumulative contribution of $u_l^+ < -2$ was nearly zero, whereas the vortex stretching within $u_l^+ > 2$ was responsible for 15 % of the contribution to C_{f2}; the cumulative contribution of $u_l^+ < -1$ and $u_l^+ > 1$ was 11 % and 36 %, respectively. The intense spanwise motion of the positive u_l in the near-wall region enhanced the small-scale velocity fluctuations as well as the vortical motions, which were related to the intense vortex-stretching effect. As a result, the amplification effect by the positive-u_l structure considerably contributed to the skin friction, in contrast to the negative-u_l structures, and thus manipulating the near-wall spanwise motions induced by outer large-scale structures could offer a new strategy for controlling turbulence.

6.1. *Analysis of a drag-reduced turbulent flow*

The AM effect of the large-scale structures on the vortical motions was quantified by integrating the wall-normal distribution of $\langle -w\omega_y\rangle$ according to the strength of u_l in (6.5). The contribution of the AM to C_f was varied according to the strength of u_l. In particular, the frictional drag induced by the positive-u_l event was significantly larger than that by the negative-u_l event. To explore further, a drag-reduced turbulent flow was examined. We used two DNS datasets for the turbulent channel with no-slip and

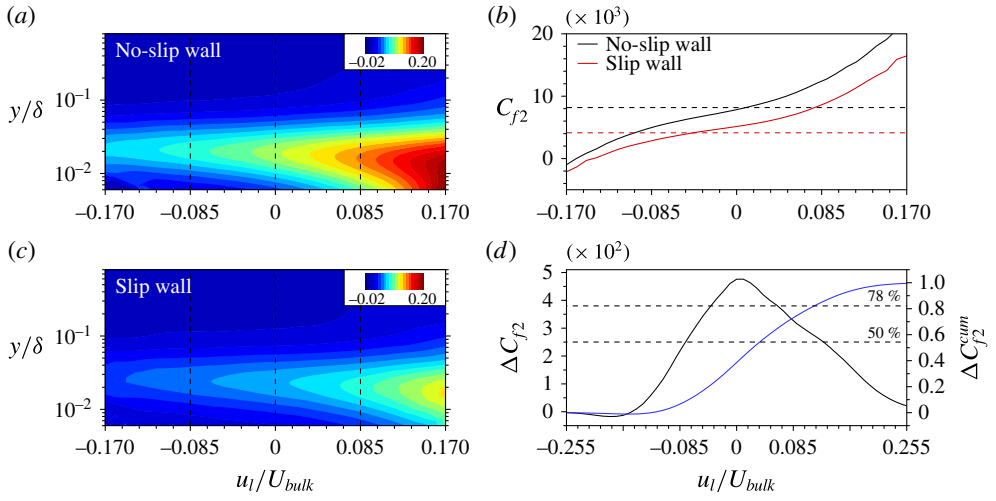

FIGURE 14. (Colour online) (*a*,*c*) Correlation between the spanwise velocity fluctuations and the wall-normal velocity fluctuations conditioned on the large-scale fluctuations along the wall-normal direction, $\langle -w\omega_y(u_l,\, y)\rangle\delta/U_{bulk}^2$: (*a*) no-slip wall; (*c*) slip wall. (*b*) Dependence of the skin friction induced by $\langle -w\omega_y(u_l,\, y)\rangle$ on the large-scale fluctuations, $\langle C_{f2}(u_l)\rangle$. The dashed lines represent C_{f2} in (6.1). (*d*) Contribution of the change in $\langle C_{f2}(u_l)\rangle$ to the reduced C_{f2}, ΔC_{f2} (black) and cumulative distribution of $\Delta C_{f2}(u_l)$, ΔC_{f2}^{cum} (blue).

slip condition at a given bulk Reynolds number $Re_b = U_{bulk}\delta/\nu = 10\,333$ (Yoon *et al.* 2016*b*). Although the drag reduction was achieved due to the slip boundary condition, we can examine the variation of the skin friction induced by the modulated vortical motions in the drag-reduced flow – especially the high skin friction under the large-scale high-speed structures observed in figure 13. This approach could provide an evidence of controlling the AM effect on C_f by manipulating the high-speed structures. Figure 14(*a*,*c*) shows the contours of $\langle -w\omega_y(u_l, y)\rangle$ for the no-slip and slip wall. Here, the quantities were normalized by the bulk mean velocity U_{bulk} and the channel half-height δ. At the no-slip wall, $u_l/U_{bulk} = 0.17$ was consistent with $u_l^+ = 3$. Irrespective of u_l, the magnitude of $\langle -w\omega_y(u_l, y)\rangle$ in figure 14(*c*) was lower than that in figure 14(*a*). The vortex-stretching force decreased in the channel flow with the slip condition. Note that the overall drag under the slip condition was reduced by 35 % relative to the flow with the no-slip condition (Yoon *et al.* 2016*b*). In other words, the reduced magnitude of the vortex-stretching force, which was affected by the large-scale low- and high-speed events, contributed to the overall drag reduction in the slip wall.

The influence of the large-scale motions on the skin friction under the no-slip and slip wall was compared by plotting $\langle C_{f2}(u_l)\rangle$ (6.4) for each case in figure 14(*b*). The horizontal dashed lines in figure 14(*b*) represent the contribution of $\langle -w\omega_y\rangle$ to the total C_f; the second term on the right-hand side of (6.1) for the no-slip ($C_{f2,n}$) and slip wall ($C_{f2,s}$). Although the plot of $\langle C_{f2}(u_l)\rangle$ for the slip wall fell below that for the no-slip wall, the difference in $\langle C_{f2}(u_l)\rangle$ between the no-slip and slip wall varied with the strength of u_l. For the intense negative u_l ($u_l/U_{bulk} \approx -0.17$), there was a slight difference in $\langle C_{f2}(u_l)\rangle$ between the no-slip and slip wall. However, the difference started to become noticeable as u_l increased. Above $u_l/U_{bulk} > 0.1$, in particular, the difference in $\langle C_{f2}(u_l)\rangle$ exceeded the reduced C_{f2} ($= C_{f2,n} - C_{f2,s} \approx 4.1 \times 10^{-3}$). The

skin friction induced by the vortex-stretching effect decreased at the slip wall, but the amount of change in the skin friction was significant for the positive u_l. To further explore this observation, the contribution of the change in $\langle C_{f2}(u_l)\rangle$ to the reduced C_{f2} was defined as,

$$\Delta C_{f2}(u_l) = \frac{C_{f2,n}C^{con}_{f2,n}(u_l) - C_{f2,s}C^{con}_{f2,s}(u_l)}{C_{f2,n} - C_{f2,s}}, \tag{6.8}$$

where $C^{con}_{f2,n}$ and $C^{con}_{f2,s}$ are the contributions of $\langle C_{f2}(u_l)\rangle$ to C_{f2} (6.5) for the no-slip and slip walls, respectively. $\Delta C_{f2}(u_l)$ indicates the difference in the frictional drag induced by u_l between the no-slip and slip walls and its contribution to the reduced C_f. The black line in figure 14(*d*) represents $\Delta C_{f2}(u_l)$. Although the contribution to the reduced C_{f2} was largest in the vicinity of $u_l \approx 0$, $\Delta C_{f2}(u_l)$ was not symmetric with respect to $u_l \approx 0$. As the magnitude of u_l increased, $\Delta C_{f2}(u_l)$ for $u_l < 0$ declined to a greater extent than $\Delta C_{f2}(u_l)$ for $u_l > 0$. This behaviour was evident in the cumulative distribution of $\Delta C_{f2}(u_l)$ in figure 14(*d*). For the intense positive u_l region, $u_l/U_{bulk} > 0.1$ ($u_l^+ > 2$), the reduction in the skin friction induced by the amplified vortical motions was responsible for 22 % of the reduced C_{f2}; cf. for $u_l/U_{bulk} > 0.05$, $\Delta C^{cum}_{f2} = 0.6$. This result indicated that the amplification of the vortical motions within the footprint of positive u_l was markedly diminished compared to the attenuation effect produced by the negative u_l, which ultimately contributed to the total drag reduction at the slip wall. In this manner, manipulating the positive-u_l structure, which amplified the near-wall motions through the associated intense spanwise motions (§ 5) might provide a means for controlling turbulence. The analysis described in this section serves as a reliable measure for evaluating new control strategies by manipulating the AM effects of large-scale motions.

7. Conclusions

We investigated the influence of large-scale low- and high-speed structures on the vortical motions. This influence was ultimately related to the dependence of the local skin friction on the large-scale structures. The large-scale streamwise velocity fluctuations (u_l) were extracted by employing a spanwise wavelength filter ($\lambda_z/\delta > 0.5$). The r.m.s. of the streamwise and wall-normal swirling strengths (λ_x and λ_y) was conditionally sampled as a function of the strength of u_l. The amplitudes of the swirling strengths were found to be affected by the strength of u_l. The swirling strengths were attenuated or amplified under negative or positive u_l in the near-wall region, respectively. This trend was reversed above $y^+ \approx 100$. Although the vortical motions within the positive-u_l footprint were comparable in size to the vortices observed within the negative-u_l footprint, the intense vortices under the influence of the high-speed region were relatively short in the streamwise direction with a steep inclination angle. The asymmetric influence of the large scales on the near-wall region arose from the associated spanwise motions within the footprints of u_l induced by the outer ejection ($u_l < 0$) and sweep ($u_l > 0$) motions. The near-wall spanwise velocity of positive u_l were more intense than that of negative u_l because the spanwise motions under the footprint of negative u_l decreased as the flows approached one another, whereas the sweep of the high-momentum fluid toward the wall involved a significant reduction in v and splatted on the wall, leading to an intense spanwise momentum. Conditionally averaged velocity fields associated with the vortical structures under the footprints of negative and positive u_l revealed that the modulated swirling motions lay within the induced spanwise motions of the

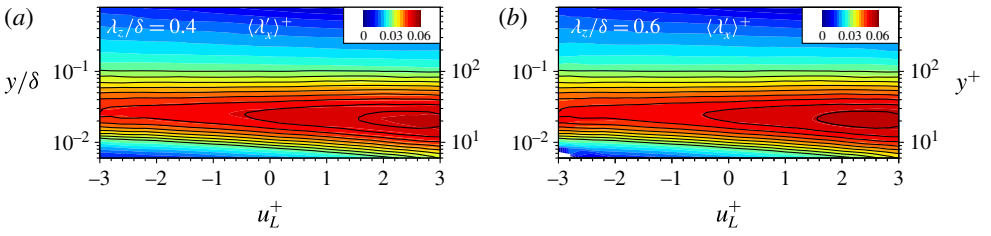

FIGURE 15. (Colour online) The r.m.s of the streamwise swirling strength (λ_x') conditioned on the large-scale fluctuations along the wall-normal direction $\langle\lambda_x'(u_l, y)\rangle^+$. The cutoff wavelengths are (*a*) $\lambda_z/\delta = 0.4$ and (*b*) 0.6. The inserted line contours are $\langle\lambda_x'(u_l, y)\rangle^+$ for the cutoff wavelength $\lambda_z/\delta = 0.5$ (consistent with figure 5) and varied over the range (0.03 : 0.003 : 0.06).

large-scale structures. The intense spanwise motions under the footprint of positive u_l strengthened the small-scale spanwise velocity fluctuations (w_s) below the centre of the near-wall vortical structures compared to w_s associated with the vortical motions under the negative u_l. In addition, the streamwise and wall-normal components (u_s and v_s) were attenuated and amplified around the modulated vortical motions, which was attributed to the dependence of the swirling motions on the u_l event. We quantified the contribution of the AM of vortical motions to the skin friction by employing the decomposition method of Yoon *et al.* (2016*a*). The velocity–vorticity correlation $\langle -w\omega_y\rangle$ was the dominant contribution to the total skin friction, and in particular this term was associated with the change of size of eddies by the large-sale motions. In the near-wall region, intense values of $\langle -w\omega_y\rangle$ appeared for the positive u_l and decreased with decreasing u_l in connection with the amplification of w_s and λ_y under the positive u_l. The resultant skin friction induced by the amplified vortical motions within $u_l^+ > 2$ was responsible for 15 % of the total C_{f2}. This analysis was applied to a drag-reduced flow, revealing that the amplification of the vortical motions within the footprint of the positive u_l was markedly diminished (more than 22 %) compared to the attenuation effect by the negative u_l, which ultimately contributed to the total drag reduction at the slip wall. These results point toward the conclusion that manipulating the positive-u_l structure, which amplified the near-wall motions through the intense spanwise motions, may provide a means for controlling the turbulence and that computing the contribution of $\langle -w\omega_y\rangle$ to the skin friction offers a reliable measure for evaluating new control strategies using the AM behaviour of large-scale motions.

Acknowledgements

This work was supported by the Creative Research Initiatives (no. 2017-013369) program of the National Research Foundation of Korea (MSIP) and supported by the Supercomputing Center (KISTI).

Appendix A. Effect of the cutoff wavelength

The influence of the cutoff wavelength adopted in the scale decomposition was addressed by re-evaluating the conditional statistics at $\lambda_z/\delta = 0.4$ and 0.6. The filled contours in figure 15 represent $\langle\lambda_x'(u_l, y)\rangle^+$. As the cutoff wavelength increased, the number of large-scale events with a large magnitude decreased. The general trend remained unchanged. Regardless of the cutoff wavelength, the amplitudes of λ_x

increased with increasing strength of u_l in the near-wall region, and this was reversed in the outer region. The peak remained present at a similar wall-normal position. For $u_l^+ = 2$, the peak of $\langle \lambda_x'(u_l, y)\rangle^+$ was located at $y^+ = 20$. As the wall-normal position increased, the sign of the relative difference $\Delta\lambda_x'$ (4.3) changed at $y^+ \approx 100$, regardless of the cutoff wavelength. The reverse of the AM effect of u_l on the streamwise swirling strength remained unchanged for the streamwise swirling strength.

Appendix B. Velocity fields with a low strength of the large-scale events

B.1. *Conditional structures of the small scales*

We examined the velocity fields related to weak u_l ($u_l^+ \approx 0$) in the near-wall region to clarify whether this condition indicated the absence of outer large-scale events. As noted in § 4, the small-scale variances in the $u_l^+ = 0$ bin indicated unmodulated small scales due to the weak strength of the carrier signal u_l^+. Here, a weak u_l was chosen with a magnitude less than 0.2 ($|u_l^+| < 0.2$), corresponding to the $u_l^+ = 0$ bin of the conditional sampling method (§ 3). The conditionally averaged velocities for the weak negative- and positive-u_l events ($\langle \boldsymbol{u}|^{ns}\rangle$ and $\langle \boldsymbol{u}|^{ps}\rangle$) were defined as

$$\langle \boldsymbol{u}|^{ns}(r_x, y, r_z)\rangle = \langle \boldsymbol{u}(x + r_x, y, z + r_z)| - 0.2 < u_l^+(x, y_{ref}, z) < 0\rangle, \tag{B 1}$$

$$\langle \boldsymbol{u}|^{ps}(r_x, y, r_z)\rangle = \langle \boldsymbol{u}(x + r_x, y, z + r_z)|0 < u_l^+(x, y_{ref}, z) < 0.2\rangle, \tag{B 2}$$

where the reference wall-normal position was located at $y_{ref}^+ = 14.5$. Figure 16 illustrates the isosurfaces of $\langle u|^{ns}\rangle^+$ and $\langle u|^{ps}\rangle^+$. The conditional structures represented the low- and high-speed streaks in the near-wall region. The streamwise and spanwise extents were of the order of 1000 and 100 wall units, respectively. In particular, the streamwise length of the negative-u structures exceeded 900 wall units, whereas that of the positive-u structures was less than 700 wall units. The low-speed streaks were longer than the high-speed streaks in the near-wall region. In addition, these near-wall structures included a pair of roll motions, the centres of which were located at $y^+ = 30$ in figure 16(*c*,*d*). Although the reference wall-normal position was $y_{ref}^+ = 14.5$, the conditional structures associated with the footprints (figure 7) displayed long streamwise lengths and extended beyond the near-wall region. The small-scale condition used in the present study was not relevant to the outer events.

B.2. *Conditional structure of the vortical structures*

The conditional vortical structures were examined under the influence of outer large-scale structures in § 5.2, by conditioning the streamwise swirling strength at the weak u_l, and the associated velocity fields were conditionally averaged. The streamwise swirling strength under the weak-u_l event was conditionally averaged,

$$\langle \lambda_x|^{ss}(r_x, y, r_z)\rangle = \langle \lambda_x(x + r_x, y, z + r_z)| - 0.2 < u_l^+(x, y_{ref}, z) < 0.2\rangle. \tag{B 3}$$

Figure 17(*a*) plots $\langle \lambda_x|^{ss}\rangle$. The conditional structure of $\langle \lambda_x|^{ss}\rangle$ featured a streamwise extent of approximately 200 wall units with an inclination angle of 9.1°, consistent with the results of Jeong *et al.* (1997). The maximum value of $\langle \lambda_x|^{ss}\rangle^+$ was 0.06, which was intermediate between the negative- and positive-u_l events plotted in figures 8. The attenuation or amplification of the swirling strength shown in § 5.2 was a unique feature under the footprints of the large-scale events.

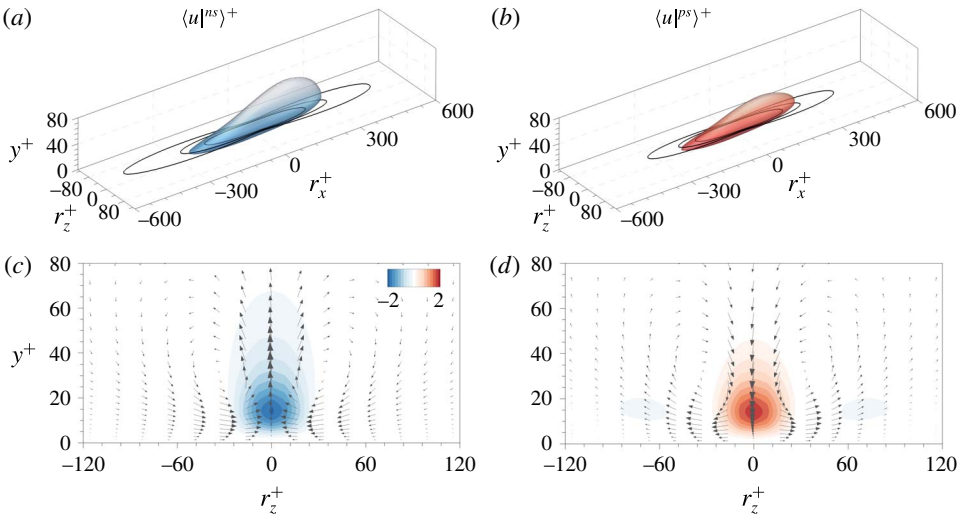

FIGURE 16. (Colour online) Conditional structures associated with the near-wall structures at $y^+ = 14.5$. (*a*,*b*) Isosurfaces of the streamwise velocity fluctuations $\langle u|^{ns}\rangle^+ = -0.5$ (blue) and $\langle u|^{ps}\rangle^+ = 0.5$ (red). The line contours represent $\langle u|^{ns}\rangle^+ = -0.2$, -0.4 and -0.6, and $\langle u|^{ps}\rangle^+ = 0.2$, 0.4 and 0.6 at $y = y_{ref}$. Contours of the streamwise velocity fluctuations (*c*) $\langle u|^{ns}\rangle^+$ and (*d*) $\langle u|^{ps}\rangle^+$ in the cross-stream plane ($r_x/\delta = 0$). The contours range from ± 0.4 to ± 2.0 with an increment of 0.2. The inserted vectors represent the conditionally averaged velocity of the cross-stream components.

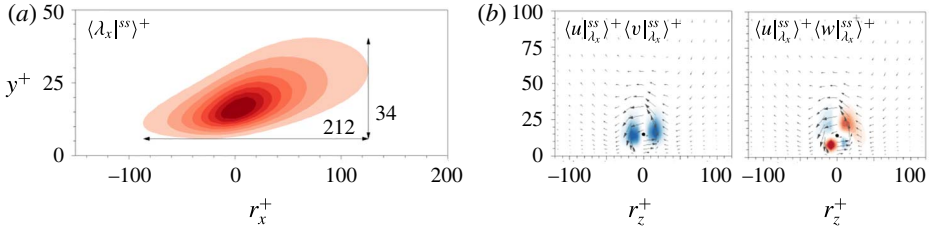

FIGURE 17. (Colour online) Contours of (*a*) $\langle \lambda_x|^{ss}\rangle^+$ in the x–y plane ($r_z/\delta = 0$). The contours represent the conditioned swirling strength normalized by its maximum value. The filled contour levels are consistent with figure 8. (*b*) $\langle u|^{ss}_{\lambda_x}\rangle\langle v|^{ss}_{\lambda_x}\rangle$ and $\langle u|^{ss}_{\lambda_x}\rangle\langle w|^{ss}_{\lambda_x}\rangle$ in the cross-stream plane ($r_x^+ = 0$). Vectors indicate the in-plane velocity components. The filled contour levels are consistent with figures 11 and 12.

The total velocity fluctuations ($\boldsymbol{u}$) associated with the weak-u_l condition were conditionally averaged,

$$\langle \boldsymbol{u}|^{ss}_{\lambda_x}(r_x, y, r_z)\rangle = \langle \boldsymbol{u}(x + r_x, y, z + r_z)|\lambda_x(x, y_{ref}, z) > 0 \text{ and } |u_l^+(x, y_{ref}, z)| < 0.2\rangle. \quad \text{(B 4)}$$

Figure 17(*b*) shows the cross-stream plane of the educed velocity fields. The filled contours represent the coherent Reynolds stresses ($\langle u|^{ss}_{\lambda_x}\rangle\langle v|^{ss}_{\lambda_x}\rangle$ and $\langle u|^{ss}_{\lambda_y}\rangle\langle w|^{ss}_{\lambda_y}\rangle$), and the inserted vectors indicate the wall-normal and spanwise velocity fluctuations. The total velocity fields plotted in figure 17 show an absence of large-scale features, as described in § 5.2 under the weak-u_l condition. The educed flow fields conditioned at either $0 < u_l^+ < 0.2$ or $-0.2 < u_l^+ < 0$ were analogous to those presented in figure 17

because the magnitude of the large-scale components was remarkably smaller than that of the small scales (i.e. $\boldsymbol{u} \approx \boldsymbol{u}_s$ for the weak-u_l event). The educed swirling strength and associated velocity fields in figure 17 represented that the near-wall vortical structures were unaffected by the outer large-scale structures. The flow fields associated with the vortical structures under the large-scale conditions shown in § 5.2 were remarkable due to the influence of the large scales in the outer region.

REFERENCES

ABE, H., KAWAMURA, H. & CHOI, H. 2004 Very large-scale structures and their effects on the wall shear-stress fluctuations in a turbulent channel flow up to $Re_\tau = 640$. *Trans. ASME J. Fluids Engng* **126** (5), 835–843.

ADRIAN, R. J., CHRISTENSEN, K. T. & LIU, Z. C. 2000 Analysis and interpretation of instantaneous turbulent velocity fields. *Exp. Fluids* **29**, 275–290.

AGOSTINI, L. & LESCHZINER, M. A. 2014 On the influence of outer large-scale structures on near-wall turbulence in channel flow. *Phys. Fluids* **26** (7), 075107.

AHN, J., LEE, J. H., JANG, S. J. & SUNG, H. J. 2013 Direct numerical simulations of fully developed turbulent pipe flows for $Re_\tau = 180$, 544 and 934. *Intl J. Heat Fluid Flow* **44**, 222–228.

AHN, J., LEE, J. H., LEE, J., KANG, J.-H & SUNG, H. J. 2015 Direct numerical simulation of a $30R$ long turbulent pipe flow at $Re_\tau = 3008$. *Phys. Fluids* **27** (6), 065110.

DEL ÁLAMO, J. C. & JIMÉNEZ, J. 2003 Spectra of the very large anisotropic scales in turbulent channels. *Phys. Fluids* **15** (6), L41.

BALAKUMAR, B. J. & ADRIAN, R. J. 2007 Large-and very-large-scale motions in channel and boundary-layer flows. *Phil. Trans. R. Soc. Lond.* A **365** (1852), 665–681.

BANDYOPADHYAY, P. R. & HUSSAIN, A. K. M. F. 1984 The coupling between scales in shear flows. *Phys. Fluids* **27** (9), 2221–2228.

BERNARDINI, M. & PIROZZOLI, S. 2011 Inner/outer layer interactions in turbulent boundary layers: a refined measure for the large-scale amplitude modulation mechanism. *Phys. Fluids* **23** (6), 061701.

BROWN, G. L. & THOMAS, A. S. W. 1977 Large structure in a turbulent boundary layer. *Phys. Fluids* **20** (10), S243–S252.

CHAUHAN, K. A., MONKEWITZ, P. A. & NAGIB, H. M. 2009 Criteria for assessing experiments in zero pressure gradient boundary layers. *Fluid Dyn. Res.* **41** (2), 021404.

CHERNYSHENKO, S. I., MARUSIC, I. & MATHIS, R. 2012 Quasi-steady description of modulation effects in wall turbulence. arXiv:1203.3714.

CHIN, C., PHILIP, J., KLEWICKI, J., OOI, A. & MARUSIC, I. 2014 Reynolds-number-dependent turbulent inertia and onset of log region in pipe flows. *J. Fluid Mech.* **757**, 747–769.

CHUNG, D. & MCKEON, B. J. 2010 Large-eddy simulation of large-scale structures in long channel flow. *J. Fluid Mech.* **661**, 341–364.

CHUNG, D., MONTY, J. P. & OOI, A. 2014 An idealised assessment of Townsend's outer-layer similarly hypothesis for wall turbulence. *J. Fluid Mech.* **742**, R3.

DENNIS, D. J. C. & NICKELS, T. B. 2011 Experimental measurement of large-scale three-dimensional structures in a turbulent boundary layer. Part 2. Long structures. *J. Fluid Mech.* **673**, 218–244.

FISCALETTI, D., GANAPATHISUBRAMANI, B. & ELSINGA, G. E. 2015 Amplitude and frequency modulation of the small scales in a jet. *J. Fluid Mech.* **772**, 756–783.

FUKAGATA, K., IWAMOTO, K. & KASAGI, N. 2002 Contribution of Reynolds stress distribution to the skin friction in wall-bounded flows. *Phys. Fluids* **14** (11), 13–17.

GANAPATHISUBRAMANI, B., HUTCHINS, N., MONTY, J. P., CHUNG, D. & MARUSIC, I. 2012 Amplitude and frequency modulation in wall turbulence. *J. Fluid Mech.* **712**, 61–91.

GANAPATHISUBRAMANI, B., LONGMIRE, E. K. & MARUSIC, I. 2003 Characteristics of vortex packets in turbulent boundary layers. *J. Fluid Mech.* **478**, 35–46.

GUALA, M., HOMMEMA, S. E. & ADRIAN, R. J. 2006 Large-scale and very-large-scale motions in turbulent pipe flow. *J. Fluid Mech.* **554**, 521–542.

GUALA, M., METZGER, M. & MCKEON, B. J. 2011 Interactions within the turbulent boundary layer at high Reynolds number. *J. Fluid Mech.* **666**, 573–604.

HAMILTON, J. M., KIM, J. & WALEFFE, F. 1995 Regeneration mechanisms of near-wall turbulence structures. *J. Fluid Mech.* **287**, 317–348.

HOYAS, S. & JIMÉNEZ, J. 2006 Scaling of the velocity fluctuations in turbulent channels up to $Re_\tau = 2003$. *Phys. Fluids* **18** (1), 011702.

HUTCHINS, N. & MARUSIC, I. 2007*a* Evidence of very long meandering features in the logarithmic region of turbulent boundary layers. *J. Fluid Mech.* **579**, 1–28.

HUTCHINS, N. & MARUSIC, I. 2007*b* Large-scale influences in near-wall turbulence. *Phil. Trans. R. Soc. Lond.* A **365** (1852), 647–664.

HUTCHINS, N., MONTY, J. P., GANAPATHISUBRAMANI, B., NG, H. C. H. & MARUSIC, I. 2011 Three-dimensional conditional structure of a high Reynolds number turbulent boundary layer. *J. Fluid Mech.* **673**, 255–285.

HWANG, J., LEE, J. & SUNG, H. J. 2016*a* Influence of large-scale accelerating motions on turbulent pipe and channel flows. *J. Fluid Mech.* **804**, 420–441.

HWANG, J., LEE, J., SUNG, H. J. & ZAKI, T. A. 2016*b* Inner-outer interactions of large-scale structures in turbulent channel flow. *J. Fluid Mech.* **790**, 128–157.

JACOBS, R. G. & DURBIN, P. A. 2001 Simulations of bypass transition. *J. Fluid Mech.* **428**, 185–212.

JEONG, J. & HUSSAIN, F. 1995 On the identification of a vortex. *J. Fluid Mech.* **285**, 69–94.

JEONG, J., HUSSAIN, F., SCHOPPA, W. & KIM, J. 1997 Coherent structures near the wall in a turbulent channel flow. *J. Fluid Mech.* **332**, 185–214.

JIMÉNEZ, J. & PINELLI, A. 1999 The autonomous cycle of near-wall turbulence. *J. Fluid Mech.* **389**, 335–359.

KIM, K., BAEK, S. J. & SUNG, H. J. 2002 An implicit velocity decoupling procedure for the incompressible Navier–Stokes equations. *Intl J. Numer. Meth. Fluids* **38** (2), 125–138.

LEE, J. H. & SUNG, H. J. 2011 Very-large-scale motions in a turbulent boundary layer. *J. Fluid Mech.* **673**, 80–120.

LEE, J. H. & SUNG, H. J. 2013 Comparison of very-large-scale motions of turbulent pipe and boundary layer simulations. *Phys. Fluids* **25** (4), 045103.

LIU, Z., ADRIAN, R. J. & HANRATTY, T. J. 2001 Large-scale modes of turbulent channel flow: transport and structure. *J. Fluid Mech.* **448**, 53–80.

MARUSIC, I., MATHIS, R. & HUTCHINS, N. 2010 Predictive model for wall-bounded turbulent flow. *Science* **329** (5988), 193–196.

MATHIS, R., HUTCHINS, N. & MARUSIC, I. 2009 Large-scale amplitude modulation of the small-scale structures in turbulent boundary layers. *J. Fluid Mech.* **628**, 311–337.

MATHIS, R., MARUSIC, I., CHERNYSHENKO, S. L. & HUTCHINS, N. 2013 Estimating wall-shear-stress fluctuations given an outer region input. *J. Fluid Mech.* **715**, 163–180.

MONTY, J. P., STEWART, J. A., WILLIAMS, R. C. & CHONG, M. S. 2007 Large-scale features in turbulent pipe and channel flows. *J. Fluid Mech.* **589**, 147–156.

ÖRLÜ, R. & SCHLATTER, P. 2011 On the fluctuating wall-shear stress in zero pressure-gradient turbulent boundary layer flows. *Phys. Fluids* **23**, 021704.

ROBINSON, S. K. 1991 Coherent motions in the turbulent boundary layer. *Annu. Rev. Fluid Mech.* **23** (1), 601–639.

SCHLATTER, P. & ÖRLÜ, R. 2010*a* Assessment of direct numerical simulation data of turbulent boundary layers. *J. Fluid Mech.* **659**, 116–126.

SCHLATTER, P. & ÖRLÜ, R. 2010*b* Quantifying the interaction between large and small scales in wall-bounded turbulent flows: a note of caution. *Phys. Fluids* **22** (5), 051704.

SCHLATTER, P., ÖRLÜ, R., LI, Q., BRETHOUWER, G., FRANSSON, J. H., JOHANSSON, A. V., ALFREDSSON, P. H. & HENNINGSON, D. S. 2009 Turbulent boundary layers up to $Re_\theta = 2500$ studied through simulation and experiment. *Phys. Fluids* **21** (5), 51702.

SMITS, A. J., MATHESON, N. & JOUBERT, P. N. 1983 Low-Reynolds-number turbulent boundary layers in zero and favorable pressure gradients. *J. Ship Res.* **27**, 147–157.

TALLURU, K. M., BAIDYA, R., HUTCHINS, N. & MARUSIC, I. 2014 Amplitude modulation of all three velocity components in turbulent boundary layers. *J. Fluid Mech.* **746**, R1.

TENNEKES, H. & LUMLEY, J. L. 1972 *A First Course in Turbulence*. MIT Press.

TOH, S. & ITANO, T. 2005 Interaction between a large-scale structure and near-wall structures in channel flow. *J. Fluid Mech.* **524**, 249–262.

TOMKINS, C. D. & ADRIAN, R. J. 2003 Spanwise structure and scale growth in turbulent boundary layers. *J. Fluid Mech.* **490**, 37–74.

WU, X., BALTZER, J. R. & ADRIAN, R. J. 2012 Direct numerical simulation of a 30R long turbulent pipe flow at $R^+ = 685$: large- and very large-scale motions. *J. Fluid Mech.* **698**, 235–281.

YOON, M., AHN, J., HWANG, J. & SUNG, H. J. 2016*a* Contribution of velocity–vorticity correlations to the frictional drag in wall-bounded turbulent flows. *Phys. Fluids* **28** (8), 081702.

YOON, M., HWANG, J., LEE, J., SUNG, H. J. & KIM, J. 2016*b* Large-scale motions in a turbulent channel flow with the slip boundary condition. *Intl J. Heat Fluid Flow* **61**, 96–107.

ZHOU, J., ADRIAN, R. J., BALACHANDAR, S. & KENDALL, T. M. 1999 Mechanisms for generating coherent packets of hairpin vortices in channel flow. *J. Fluid Mech.* **387**, 353–396.